THE ASTROPHYSICAL JOURNAL, 466:911–937, 1996 August 1

THE ATMOSPHERES OF TYPE II SUPERNOVAE AND THE EXPANDING PHOTOSPHERE METHOD

RONALD G. EASTMAN
General Studies Group, Lawrence Livermore National Laboratory, Livermore, CA 94550
BRIAN P. SCHMIDT
Mount Stromlo and Siding Spring Observatories, The Australian National University, Private Bag, Weston Creek P.O., ACT 2611, Australia
AND
ROBERT KIRSHNER
Harvard-Smithsonian Center for Astrophysics, 60 Garden Street, Cambridge, MA 02138
Received 1995 November 30; accepted 1996 February 15

ABSTRACT

The Expanding Photosphere Method (EPM) determines distances to Type II supernova (SNe II) by comparing the photospheric angular size with the expansion velocity measured from spectral lines. The photospheres of SNe II are low density and are dominated by electron scattering, and consequently the photospheric flux is dilute relative to a Planck function at the best-fitting continuum color temperature. The reliability of EPM distances depends on understanding how the dilution is related to physical properties of the supernova atmosphere. To study this, we have calculated 63 different model atmospheres relevant to SNe II. The excitation, ionization, and thermal structure are described for the case of high effective temperature in which the atmosphere is completely ionized, and for the case of cooler effective temperatures in which the photosphere is formed in a region of recombining hydrogen. The general spectral features of both cases are discussed. We explore how the computed spectrum changes with density structure, helium abundance, metallicity, expansion rate, and luminosity or effective temperature. The most important variable in determining spectral appearance is the effective temperature. The amount by which the emergent flux is dilute relative to the best-fitting blackbody depends on a number of factors, most important of which are the temperature and, in short-wavelength bandpasses, density at the photosphere. For each of the models we derive distance correction factors for application in EPM, using the four filter combinations $\{BV\}$, $\{VI_c\}$, $\{BVI_c\}$, and $\{JHK\}$. The main differences may be expressed in terms of the observable color temperature and a slowly varying dependence on density. Functional fits to the distance correction factor are provided which can be used to estimate the photospheric angular size from broadband photometry. The effect of uncertain dust extinction on angular size is shown to be small. This work places EPM on a firm theoretical foundation and substantiates the Hubble constant measurement by Schmidt et al. of $H_0 = 73 \pm 7$.

Subject headings: radiative transfer — stars: atmospheres — stars: distances — supernovae: general

1. INTRODUCTION

The application of the Expanding Photosphere Method (EPM) of measuring distances to Type II supernovae (SNe II) is a very promising and appealing technique for determining the extragalactic distance scale and expansion rate of the universe. Type II supernovae are bright, typically $M_B \sim -17$ to -18, and visible to distances well beyond that at which cosmological recession velocity dominates over local noncosmological motion. The method provides distance measures independent of any other local or intermediate range calibrators, avoiding the accumulation of errors from the bootstrap process inherent in standard-candle techniques. Unlike other, empirically established correlations, some of which are poorly understood, the physical basis for EPM is easy to understand and, since the emitting gas is the simplest one possible (hydrogen), it can be modeled accurately with currently available information and technology.

The essential ideas of EPM have been around for more than 20 years and were first developed and implemented by Kirshner & Kwan (1974), who used EPM to obtain distance measures to SN 1969L and to SN 1970G. The basic technique, without further modifications or improvements, was also employed by Branch et al. (1983) to determine the distance to SN 1979C and to SN 1987A (Branch 1987). A related idea by Schurman, Arnett, & Falk (1979) utilized theoretical light curves by Falk & Arnett (1977) to determine the intrinsic brightness of Type II supernovae and measure the distances to SN 1969L and SN 1970G. Their results were consistent with those of Kirshner & Kwan (1974); however, the relationship between the color temperature and absolute flux was essentially the same as that employed by the others, i.e., that the radiated flux is Planckian.

The suggestion that there might be significant departures from the blackbody distribution in the emergent flux, assumed by early applications of EPM, was obvious to posit but difficult to answer quantitatively. Hershkowitz, Linder, & Wagoner (1986a, b) and Hershkowitz & Wagoner (1987) looked at the general question of flux dilution of the continuum by utilizing both analytic and numerical models of static, plane-parallel atmospheres consisting of hydrogen in detailed balance. While these models lacked the detail necessary to yield precise corrections needed for accurate application of EPM, they demonstrated many of the basic effects and established the importance of flux dilution: the flux from supernova photospheres would be less than that given by the best-fitting blackbody spec-

trum. And Chilikuri & Wagoner (1988) used the numerical results of Hershkowitz et al. (1986b) and Hershkowitz & Wagoner (1987) to determine the distance to SN 1987A

Faster computers have made it feasible to run more sophisticated codes which produce realistic custom atmosphere fits to observations of individual supernovae, yielding more accurate distance estimates with EPM. The most notable application has been to supernova 1987A in the Large Magellanic Cloud (LMC) by Eastman & Kirshner (1989), Schmutz et al. (1990), and Höflich (1991). The LMC distances found in these studies all agreed to $\pm 10\%$.

Schmidt, Kirshner, & Eastman (1992) used a hybrid approach to account for flux dilution in SNe II, combining Type II atmosphere models and optical distance correction factors (see below) derived empirically from SN 1987A, to obtain the distance to nine other extragalactic supernovae and to make a determination of the Hubble constant entirely from SNe II. Using preliminary values of the results to be presented here, Schmidt et al. (1994a) determined the distance to the most distant Type II plateau supernovae (SNe IIp) yet studied, SN 1992am at $cz = 14{,}600$ km s^{-1}. And Schmidt et al. (1994b) have used observations of five SNe II from the Cerro Tololo Inter-American Observatory (CTIO) to obtain distances which, when combined with other SNe II distance measures, have yielded an improved determination of the Hubble constant; $H_0 = 73 \pm 7$ km s^{-1} Mpc^{-1} (statistical). Since this is potentially an important, independent measurement, it seems worth the effort to examine its theoretical basis in a systematic way.

The earliest formulation of EPM (Kirshner & Kwan 1974) assumed that Type II supernovae possess a spherically symmetric expanding photosphere which radiates as a blackbody. If the redshift $z \ll 1$ and the supernova is reddened, then the flux density at the Earth, f_ν, is given by

$$f_\nu = \theta^2 \pi B_\nu(T_c) 10^{-0.4 A_\nu} , \qquad (1)$$

where $\theta \equiv R_{\rm ph}/D$ is the angular size, $R_{\rm ph}$ is the photospheric radius, D is the distance to the supernova, $B_\nu(T_c)$ is the Planck function at color temperature T_c, and A_ν is the dust extinction. The envelope undergoes free expansion, and at time t the radius of the photosphere is related to its expansion velocity by

$$R_{\rm ph} = R(m_{\rm ph}, t) \approx v(m_{\rm ph})(t - t_0) + R_0(m_{\rm ph}) , \qquad (2)$$

where $m_{\rm ph}$ is the Lagrangian mass coordinate of material instantaneously at the photosphere. The value of $v_{\rm ph}$ is determined from the shape of P Cygni absorption features, usually by the blueshift velocity of the absorption minima of weak lines. The radius of the supernova at the instant of shock breakout, $R_0(m_{\rm ph})$, can usually be ignored, since typically $R_{\rm ph} \sim 10^{15}$ cm at optical maximum ($\sim$20 days after explosion in the 15 $M_\odot$ red supergiant [RSG] model of Eastman et al. 1994), whereas $R_0 \sim 10^{13}$ cm.

For the hydrogen envelope, the part of the star most relevant for EPM, homologous expansion is a very good assumption. Roughly half the remaining shock-deposited internal energy is converted to kinetic energy for every factor of 2 increase in radius, and initially the envelope doubles in size on a timescale $t_e \sim 10^{13}$ cm/10^9 cm s^{-1} $\sim 10^4$ s. Most SNe II have doubled in size several times at the epoch of discovery. Since they are expanding freely, velocity becomes a good coordinate to use in labeling different layers of the star. An exception to this is in the core, where radioactive heating from the decay of ^{56}Ni and ^{56}Co may result in further hydrodynamic evolution following shock breakout. In a 35 $M_\odot$ RSG without mass loss, a reverse shock forms from deceleration at the H-He interface and may take several months to propagate back to the center (Herant & Woosley 1994); however, even for this extreme and probably uncommon case, the reverse shock does not affect the evolution of the outer parts of the H envelope. Since the explosion energy $E \sim 10^{51}$ ergs is much greater than the gravitational binding energy, $U \sim 10^{49}$ ergs, gravitational deceleration is unimportant. Likewise, the ejected mass, $M_{\rm ej} \gtrsim 10\ M_\odot$, greatly exceeds the swept up mass, for reasonable values of the density of circumstellar and interstellar matter, and so mass accretion will have no measurable effect on the expansion velocity during the photospheric phase (see, however, Suzuki & Nomoto 1995 for a discussion of hydrodynamic slowing in SN 1993J and other stars which have experienced substantial Roche lobe overflow prior to explosion).

We did not put a frequency subscript on θ in equation (1). Since the optical continuum opacity is dominated by electron scattering, the opacity is gray, and there is a well-defined photosphere, or surface of last scattering. This is not true in the ultraviolet ($\lambda \lesssim 4000$ Å), where the cumulative effect of many overlapping lines greatly enhances the effective opacity, or in the far-infrared, where the λ^3 dependence of the free-free opacity causes it to dominate over electron scattering at very long wavelengths. SNe IIp are characterized by an enduring phase of nearly constant or slowly varying luminosity lasting up to 150 days or more after explosion. During this phase, most of the emitted energy is in the optical continuum, and the photosphere is at a well-defined position at the inward moving recombination front.

To avoid confusion, we should note that some researchers prefer to use the term "photosphere" to describe the location at which the radiation field thermalizes to the local gas temperature (e.g., Montes & Wagoner 1995). We prefer to call that region the "thermalization depth," and we use the term "photosphere" to describe the region of total optical depth $\tau = \frac{2}{3}$, which is approximately the point at which photons escape to infinity, regardless of whether they were emitted by a scattering or thermal process.

Equation (1) is really many equations, one for each observed frequency bin, which provide the constraints needed to determine both θ and T_c. If accurate spectrophotometry is available, then one can determine θ and T_c from observations by minimizing the quantity

$$\mathscr{E} = \int_{\nu_1}^{\nu_2} [f_\nu - \theta^2 \pi B_\nu(T_c) 10^{-0.4 A_\nu}]^2 \, d\nu . \qquad (3)$$

Below we will give a different prescription for finding T_c and θ from broadband photometry, the type of measurement usually available for these events.

Having determined θ_j, the photospheric angular size at time t_j, either from spectrophotometric or broadband photometric observations, and the photospheric velocity v_j from spectra, one can write

$$\theta_j D = v_j(t_j - t_0) , \qquad (4)$$

which is a linear equation in two unknowns. Observations at two distinct epochs provide enough information to determine the distance to the supernova, D and its time of explosion, t_0, although one usually employs observations obtained at as many epochs as possible, and the best answer

can be computed by the method of least squares. The method has in it a built-in check, similar in concept to that used to test for a standard-candle relationship: although θ, T, and v all change with time, θ/v should vary linearly with t.

As alluded to earlier, the emergent flux is *not* precisely Planckian. To first order, it can be described as a *dilute* blackbody:

$$f_\nu = \theta^2 \zeta^2 \pi B_\nu(T_c) 10^{-0.4 A_\nu}, \quad (5)$$

where we have introduced a dilution factor, ζ^2 (or *distance correction factor*, ζ, since the distance derived using eq. [1] will be an overestimate by the amount $1/\zeta$). In general, $\zeta < 1$, and this has been understood for over a decade to result from the important fact that the scattering opacity due to free electrons, $\sigma_\nu \approx N_e \sigma_T$, greatly exceeds that of true continuum absorption, k_ν (Wagoner 1982). Consequently, the emergent flux at the photosphere possesses the frequency distribution of a Planck function at the local kinetic temperature of gas at the thermalization depth, $\tau_{\rm thm}$, where

$$\tau_{\rm thm} \sim \sqrt{\frac{\sigma_\nu + k_\nu}{3k_\nu}}, \quad (6)$$

and the emergent flux is diluted by an amount $\zeta^2 \approx 1/\tau_{\rm thm}$ (Mihalas 1978, p. 149; Wagoner 1982).

Another reason why ζ is expected to depart from unity is that, as in all atmospheres, the supernova photosphere is a place in which photon mean free paths exceed the distance over which the effective source function in the atmosphere changes, and the emergent spectrum contains contributions from a range of source function values. This results in limb darkening, which for SNe II photospheres will be nearly identical to that of either a gray or scattering dominated atmosphere (see, e.g., Chandrasekhar 1961, p. 125) Spherical dilution of the outward streaming radiation field may also be a factor contributing to flux dilution, especially if the thickness of the photosphere is comparable to the radius.

Accurate spectrophotometry is more difficult to obtain than broadband photometry, and the former is usually not available. Therefore, we reformulate the distance determination problem in terms of broadband fluxes. Using equation (5), the apparent magnitude in photometric band $\bar{\nu}$ (e.g., $\bar{\nu} = U, B, V, \ldots$) can be written

$$m_{\bar{\nu}} \equiv -2.5 \log \left[\int_0^\infty \phi_{\bar{\nu},\nu} f_\nu \, d\nu \right] + C_{\bar{\nu}}$$

$$\approx -2.5 \log \left[\theta^2 \zeta^2 \int_0^\infty \phi_{\bar{\nu},\nu} \pi B_\nu(T_c) d\nu \right] + C_{\bar{\nu}} + A_{\bar{\nu}}, \quad (7)$$

where $\phi_{\bar{\nu},\nu}$ is the transmission function for bandpass $\bar{\nu}$ at frequency ν, with normalization constant $C_{\bar{\nu}}$, and $A_{\bar{\nu}}$ is the broadband dust extinction. Let

$$b_{\bar{\nu}}(T) \equiv -2.5 \log \left[\int_0^\infty \phi_{\bar{\nu},\nu} \pi B_\nu(T) d\nu \right] + C_{\bar{\nu}}. \quad (8)$$

Using a set of broadband photometric magnitudes S (e.g., $S = \{B, V, I\}$), we can determine a best-fit value for $\theta\zeta_S$ and the color temperature, T_S, by minimizing the quantity

$$\mathscr{E} = \sum_{\bar{\nu} \in S} [m_{\bar{\nu}} - A_{\bar{\nu}} + 5 \log \theta\zeta_S - b_{\bar{\nu}}(T_S)]^2. \quad (9)$$

In this equation, $b_{\bar{\nu}}(T_S)$ depends only on the transmission function of bandpass $\bar{\nu}$ and on color temperature T_S. The *distance correction factor*, ζ_S, could be a complicated function of the many different properties which characterize the expanding hydrogen envelope and determine the emergent spectrum. However, one of the results which we show in this paper (§ 4) is that ζ_S is surprisingly insensitive to most such properties. Bandpass combinations involving B and V vary with color temperature at low effective temperatures. Continuum flux dilution also has a weak density dependence ($\ln \zeta \propto \gamma \ln \rho, \gamma \sim 1/11$–$1/33$ [§ 4]).

In the above discussion, we have assumed implicitly that an independent estimate is available of the amount of intervening dust extinction. The sensitivity of the angular size derived from minimizing equation (9) is discussed in § 5, where it is shown that when $T_S \lesssim 10^4$ K, $\theta\zeta_S$ is insensitive to $A_{\bar{\nu}}$.

The next level of approximation makes no assumption about the functional form of the continuum flux and instead uses custom tailored models of the atmospheres to determine its size and rate of energy output (Eastman & Kirshner 1989; Schmutz et al. 1990; Höflich 1991). This is a time-consuming and computationally demanding procedure, and the analysis presented here shows that accurate distances can be obtained through a simpler approach.

This paper presents results from 63 realistic model atmospheres for plateau phase Type II supernovae, with particular emphasis on determining the *distance correction function* ζ_S and understanding how it depends on properties of the atmosphere and color temperature. We do not take up the equally important but separate question of how best to use spectra to measure the photospheric expansion rate. That problem will be addressed in a future paper.

This paper is divided as follows: § 2 describes the input to the model calculations and includes a discussion of our assumed density structures, the atomic model, and the transport physics. Section 3 presents the thermal and ionization structure of typical atmosphere solutions and spectroscopic results for a selection of models, compares model spectra with observations of SN 1990E, and explores sensitivities of model spectra to input parameters. In § 4 we describe the results obtained from using the atmosphere models to determine ζ_S, in § 5 we explore the effect of uncertainties in the extinction corrections to distance determinations, and we conclude in § 6.

2. PHYSICAL ASSUMPTIONS AND APPROXIMATIONS

2.1. *Overview*

The evolution of a typical Type II plateau supernova is described in some detail by several authors (Grassberg, Imshennik, & Nadyozhin 1971; Chevalier 1976; Falk & Arnett 1977; Woosley & Weaver 1986). And more recently, Eastman et al. (1994, hereafter EWWP) used a multigroup radiation transport code to show that good agreement is obtained between the broadband photometric light curves computed for the explosion of a 15 $M_\odot$ RSG and observations of the SN IIp SN 1990E.

For our present purpose, it is convenient to distinguish two phases of photospheric evolution. The first starts as the shock wave which originated at the center breaks out at the surface and covers the initial period of cooling from the breakout temperature ($\sim 10^5$ K) down to the recombination temperature of hydrogen (~ 5000 K). The second phase is an enduring era of recombination which, in RSG explosions, gives rise to the extended plateau observed in SNe IIp light curves. In the 15 $M_\odot$ IIp model studied in EWWP, the

plateau phase lasted from ~20 days until the onset of transparency at ~140 days. Beyond the plateau phase, the bolometric light curve tracks the instantaneous energy input rate from radioactive decay, the electron scattering optical depth is of order unity, and it is no longer possible to obtain accurate distances with EPM. It is the first two, optically thick phases, which concern us here.

Our model for a photospheric phase Type II supernova atmosphere is a hydrogen-dominated, optically thick, homologously expanding shell, moving at velocities $\sim 10^8$–10^9 cm s^{-1}, through which radiation diffuses to the surfaces and then escapes. We assume that shock deposited energy powers the light curve and that heat produced in the decay of radioisotopes is thermalized well inside the photosphere. Until radioactive decay heat diffuses to the surface, the luminosity arises from a narrow, well-defined region, the *diffusion depth*, of optical depth $\tau_{\rm diff}$ (see § 4 and eq. [19]). At lower optical depths, the flux divergence in the comoving frame is negligibly small, and this allows us to model the region in which $\tau < \tau_{\rm diff}$ with constant comoving frame luminosity. One of the parameters specifying an atmosphere model is therefore the comoving frame luminosity. The accuracy of this picture is discussed in § 4. Through this atmospheric layer, we solve a series of monochromatic comoving frame equations of radiative transfer, modified to take into account the time-dependent evolution of the radiation field and coupled to a gas equation of state given by the constraints of statistical and thermal equilibrium. An iterative technique is used to solve these equations, and once convergence is obtained, the transfer solution in the comoving frame is Lorentz transformed into the observer frame and used to compute the observer frame spectrum for comparison with observations. Some of the details of the explosion models, physical assumptions, and techniques used are given below.

2.2. *Density Structures*

The density structures studied include both realistic explosion models and power-law density structures in which $\rho = \rho_{15} r_{15}^{-n}$ ($r_{15} \equiv r/10^{15}$ cm). At $t \gtrsim 10$ days after explosion, the spectra computed with these simple density structures do not reproduce the SNe IIp observations as well as models based on hydrodynamic calculations of the explosion of realistic progenitor stars (see § 3), but these density distributions are a good representation of the very outmost part of the envelope in which the photosphere is located during the early plateau phase. In addition to power laws, we have also studied several exponential atmosphere density structures, where density is given by

$$\rho(r) = \rho_0 \exp\left[-(r - r_0)/dr_0\right] . \quad (10)$$

More realistic density models include models s15s2a and s25n2a of Weaver & Woosley (1993). The former had a 15 $M_\odot$ RSG progenitor, while the latter is from a 25 $M_\odot$ RSG progenitor, both of which were computed by Weaver & Woosley with the one-dimensional hydrodynamic/nucleosynthesis stellar evolution code KEPLER (Weaver, Zimmerman, & Woosley 1978; Woosley & Weaver 1986). We include also results for the KEPLER model 10hmm (Pinto & Woosley 1988), an 18 $M_\odot$ blue supergiant (BSG) model crafted to reproduce observations of SN 1987A.

Table 1 summarizes properties of the power-law atmospheres: listed in columns (2) and (4) are the density index $n \equiv -d\ln\rho/d\ln r$ and density constant; column (3) lists the age after explosion, and columns (5) and (6) list the mass density and electron density at the photosphere, $\tau = \frac{2}{3}$.

TABLE 1

PARAMETERS OF POWER LAW ATMOSPHERES

Model	n	age [days]	ρ_{15}† [gm cm^{-3}]	ρ_{ph} [gm cm^{-3}]	$N_{e,ph}$ [cm^{-3}]	R_{ph} [cm]	V_{max} [cm s^{-1}]	V_{min} [cm s^{-1}]	V_{ph} [cm s^{-1}]	Lum [ergs s^{-1}]	Y	Z	non-LTE
(1)	(2)	(3)	(4)	(5)	(6)	(7)	(8)	(9)	(10)	(11)	(12)	(13)	(14)
p6.10.1	6	10	1.61×10^{-14}	9.08×10^{-15}	4.42×10^{9}	1.1×10^{15}	3.0×10^{9}	6.4×10^{8}	1.3×10^{9}	3.0×10^{42}	0.25	1.00	H
p6.10.2	6	10	1.61×10^{-14}	9.08×10^{-15}	5.23×10^{9}	1.1×10^{15}	2.0×10^{9}	6.4×10^{8}	1.3×10^{9}	3.0×10^{42}	0.25	1.00	H, He
p6.40.1	6	40	6.62×10^{-11}	2.71×10^{-13}	4.10×10^{9}	2.5×10^{15}	1.5×10^{9}	6.0×10^{8}	7.2×10^{8}	1.8×10^{42}	0.25	1.00	H
p6.40.2	6	40	1.32×10^{-11}	1.81×10^{-14}	2.83×10^{9}	3.0×10^{15}	1.5×10^{9}	6.0×10^{8}	8.7×10^{8}	3.5×10^{42}	0.25	1.00	H
p6.40.3	6	40	3.31×10^{-11}	1.07×10^{-13}	3.84×10^{9}	2.6×10^{15}	1.5×10^{9}	6.0×10^{8}	7.5×10^{8}	2.3×10^{42}	0.25	1.00	H
p6.60.1	6	60	1.28×10^{-11}	2.65×10^{-14}	2.58×10^{9}	2.8×10^{15}	1.5×10^{9}	3.8×10^{8}	5.4×10^{8}	2.7×10^{42}	0.30	1.00	H
p6.60.2	6	60	1.28×10^{-11}	3.29×10^{-14}	2.38×10^{9}	2.7×10^{15}	1.5×10^{9}	3.8×10^{8}	5.2×10^{8}	2.5×10^{42}	0.30	1.00	H
p6.60.3	6	60	1.28×10^{-11}	2.65×10^{-14}	2.07×10^{9}	2.8×10^{15}	1.5×10^{9}	3.8×10^{8}	5.4×10^{8}	2.8×10^{42}	0.30	0.30	H
p6.60.4	6	60	1.28×10^{-11}	3.29×10^{-14}	2.41×10^{9}	2.7×10^{15}	1.5×10^{9}	3.8×10^{8}	5.2×10^{8}	2.6×10^{42}	0.30	3.00	H
p6.60.5	6	60	3.52×10^{-11}	1.44×10^{-13}	3.21×10^{9}	2.5×10^{15}	1.5×10^{9}	3.8×10^{8}	4.8×10^{8}	1.9×10^{42}	0.30	1.00	H
p6.60.6	6	60	1.28×10^{-11}	2.65×10^{-14}	2.58×10^{9}	2.8×10^{15}	1.5×10^{9}	3.8×10^{8}	5.4×10^{8}	2.7×10^{42}	0.30	1.00	H
p9.10.1	9	10	1.66×10^{-14}	1.66×10^{-14}	8.05×10^{9}	1.0×10^{15}	2.0×10^{9}	7.5×10^{8}	1.2×10^{9}	3.6×10^{42}	0.25	1.00	H
p9.10.2	9	10	1.66×10^{-14}	1.66×10^{-14}	8.17×10^{9}	1.0×10^{15}	2.0×10^{9}	7.5×10^{8}	1.2×10^{9}	3.6×10^{42}	0.25	1.00	H, He
p9.10.3	9	10	1.66×10^{-14}	1.66×10^{-14}	8.38×10^{9}	1.0×10^{15}	2.0×10^{9}	7.5×10^{8}	1.2×10^{9}	3.6×10^{42}	0.40	1.00	H, He
p9.10.4	9	10	1.66×10^{-14}	1.66×10^{-14}	8.18×10^{9}	1.0×10^{15}	2.0×10^{9}	7.5×10^{8}	1.2×10^{9}	5.0×10^{42}	0.40	1.00	H
p9.60.1	9	60	1.85×10^{-10}	6.99×10^{-14}	3.38×10^{9}	2.4×10^{15}	1.5×10^{9}	3.8×10^{8}	4.6×10^{8}	2.2×10^{42}	0.30	1.00	H
p12.10.1	12	10	1.47×10^{-14}	2.40×10^{-14}	1.12×10^{10}	9.6×10^{14}	2.0×10^{9}	8.0×10^{8}	1.1×10^{9}	3.0×10^{42}	0.25	1.00	H
p12.10.2	12	10	1.47×10^{-14}	2.40×10^{-14}	1.15×10^{10}	9.6×10^{14}	2.0×10^{9}	8.0×10^{8}	1.1×10^{9}	3.0×10^{42}	0.25	1.00	H, He
p12.10.3	12	10	7.35×10^{-16}	3.21×10^{-14}	1.50×10^{10}	7.3×10^{14}	2.0×10^{9}	6.1×10^{8}	8.4×10^{8}	3.0×10^{42}	0.25	1.00	H
p12.10.4	12	15	1.27×10^{-12}	2.24×10^{-14}	7.62×10^{9}	1.4×10^{15}	2.0×10^{9}	8.0×10^{8}	1.1×10^{9}	3.0×10^{42}	0.25	1.00	H
p12.10.5	12	10	1.47×10^{-14}	2.72×10^{-14}	1.15×10^{10}	9.5×10^{14}	2.0×10^{9}	8.0×10^{8}	1.1×10^{9}	5.0×10^{42}	0.40	1.00	H
p12.10.6	12	10	1.47×10^{-14}	2.72×10^{-14}	1.15×10^{10}	9.5×10^{14}	2.0×10^{9}	8.0×10^{8}	1.1×10^{9}	8.0×10^{42}	0.40	1.00	H
p12.10.7	12	10	1.47×10^{-14}	2.72×10^{-14}	1.15×10^{10}	9.5×10^{14}	2.0×10^{9}	8.0×10^{8}	1.1×10^{9}	1.0×10^{43}	0.40	1.00	H
p12.10.8	12	10	1.47×10^{-14}	2.72×10^{-14}	1.16×10^{10}	9.5×10^{14}	2.0×10^{9}	8.0×10^{8}	1.1×10^{9}	5.0×10^{42}	0.40	1.00	H, He
p12.10.9	12	10	1.47×10^{-14}	2.72×10^{-14}	1.15×10^{10}	9.5×10^{14}	2.0×10^{9}	8.0×10^{8}	1.1×10^{9}	8.0×10^{42}	0.40	1.00	H, He
p12.10.10	12	10	1.47×10^{-14}	3.09×10^{-14}	1.17×10^{10}	9.4×10^{14}	2.0×10^{9}	8.0×10^{8}	1.1×10^{9}	3.0×10^{43}	0.40	1.00	H, He
p12.10.11	12	10	1.47×10^{-14}	4.00×10^{-14}	1.22×10^{10}	9.2×10^{14}	2.0×10^{9}	8.0×10^{8}	1.1×10^{9}	3.0×10^{42}	0.60	1.00	H, He
p12.60.1	12	60	2.22×10^{-09}	1.01×10^{-13}	5.48×10^{9}	2.3×10^{15}	1.5×10^{9}	3.8×10^{8}	4.4×10^{8}	2.2×10^{42}	0.30	1.00	H

† $\rho(r) = \rho_{15}(r/10^{15}\ {\rm cm})^{-n}$

Since the optical continuum opacity is dominated by electron scattering, τ is effectively the same as the Thomson scattering optical depth. Column (7) lists the radius of the photosphere, columns (8), (9), and (10) list the velocity of the fastest moving gas, the velocity of the inner boundary (§ 4 below), and the velocity of the photosphere. The luminosity in the comoving frame (§ 4) is listed in column (11).

Figure 1 shows density as a function of radius for models s15s2a and s25n2a. Table 2 summarizes properties of atmospheres based upon KEPLER models and the exponential atmosphere models: column (2) lists the age after explosion, columns (3) and (4) list the mass density and electron density at the photosphere, column (5) lists the radius of the photosphere, columns (6), (7), and (8) list the velocity of the fastest moving gas, the velocity of the inner boundary, and the velocity of the photosphere, and column (9) lists the comoving frame luminosity.

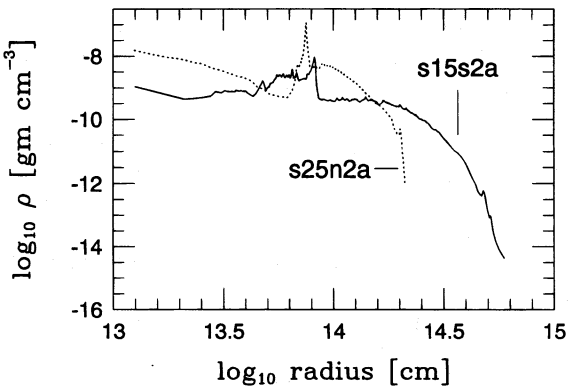

FIG. 1.—Density structure of KEPLER models s15s2a and s25s2a, both at 5 days after explosion.

TABLE 2

PARAMETERS OF NON-POWER-LAW ATMOSPHERES

Model	age [days]	ρ_{ph} [gm cm^{-3}]	$N_{e,ph}$ [cm^{-3}]	R_{ph} [cm]	V_{max} [cm s^{-1}]	V_{min} [cm s^{-1}]	V_{ph} [cm s^{-1}]	Lum [ergs s^{-1}]	Y	Z	non-LTE	notes
(1)	(2)	(3)	(4)	(5)	(6)	(7)	(8)	(9)	(10)	(11)	(12)	(13)
s15s2a models												
s15.5.1	5	3.37×10^{-13}	4.10×10^{10}	5.1×10^{14}	1.5×10^{9}	1.1×10^{9}	1.2×10^{9}	4.8×10^{42}	0.40	1.00	H, He	
s15.12.1	12	2.89×10^{-14}	1.39×10^{10}	1.2×10^{15}	1.6×10^{9}	9.1×10^{8}	1.1×10^{9}	6.0×10^{42}	0.25	1.00	H, He	
s15.12.2	12	2.75×10^{-14}	1.24×10^{10}	1.2×10^{15}	1.6×10^{9}	9.2×10^{8}	1.1×10^{9}	6.0×10^{42}	0.40	1.00	H, Ca, Fe	
s15.12.3	12	2.85×10^{-14}	1.31×10^{10}	1.2×10^{15}	1.6×10^{9}	8.9×10^{8}	1.1×10^{9}	4.1×10^{42}	0.25	1.00	H	
s15.12.4	12	2.88×10^{-14}	1.40×10^{10}	1.2×10^{15}	1.4×10^{9}	9.1×10^{8}	1.1×10^{9}	8.0×10^{42}	0.25	1.00	H	
s15.12.5	12	2.73×10^{-14}	1.23×10^{10}	1.2×10^{15}	1.5×10^{9}	9.2×10^{8}	1.1×10^{9}	8.3×10^{42}	0.25	1.00	H, Ca, Fe	
s15.19.1	19	1.58×10^{-14}	7.08×10^{9}	1.8×10^{15}	1.5×10^{9}	8.4×10^{8}	1.1×10^{9}	3.4×10^{42}	0.25	1.00	H	
s15.19.2	19	1.64×10^{-14}	7.37×10^{9}	1.7×10^{15}	1.4×10^{9}	8.4×10^{8}	1.1×10^{9}	4.6×10^{42}	0.25	1.00	H	
s15.19.3	19	1.92×10^{-14}	7.65×10^{9}	1.7×10^{17}	1.4×10^{9}	7.5×10^{8}	1.0×10^{9}	3.9×10^{42}	0.40	1.00	H, Ca, Fe	
s15.19.4	19	1.94×10^{-14}	7.65×10^{9}	1.7×10^{15}	1.4×10^{9}	7.5×10^{8}	1.0×10^{9}	4.2×10^{42}	0.40	0.10	H, Ca, Fe	
s15.19.5	19	1.43×10^{-14}	6.46×10^{9}	1.6×10^{15}	1.1×10^{9}	6.2×10^{8}	9.5×10^{8}	4.6×10^{42}	0.25	1.00	H	a
s15.19.6	19	1.38×10^{-14}	6.50×10^{9}	1.6×10^{15}	1.1×10^{9}	6.2×10^{8}	9.6×10^{8}	6.0×10^{42}	0.25	1.00	H	a
s15.20.1	20	1.76×10^{-14}	6.91×10^{9}	1.8×10^{15}	1.5×10^{9}	8.5×10^{8}	1.1×10^{9}	3.7×10^{42}	0.40	1.00	H, Na, Ca	
s15.28.1	28	2.15×10^{-14}	7.17×10^{9}	2.3×10^{15}	1.6×10^{9}	7.0×10^{8}	9.4×10^{8}	2.9×10^{42}	0.40	1.00	H, Ca, Fe	
s15.28.2	28	1.59×10^{-14}	6.14×10^{9}	2.3×10^{15}	1.4×10^{9}	7.0×10^{8}	9.7×10^{8}	3.6×10^{42}	0.40	1.00	H, Ca, Fe	
s15.28.3	28	1.26×10^{-14}	5.46×10^{9}	2.5×10^{15}	1.5×10^{9}	7.1×10^{8}	1.0×10^{9}	3.8×10^{42}	0.25	1.00	H	
s15.28.4	28	1.32×10^{-14}	5.90×10^{9}	2.2×10^{15}	1.2×10^{9}	5.4×10^{8}	9.0×10^{8}	3.7×10^{42}	0.25	1.00	H	b
s15.28.5	28	1.44×10^{-14}	6.03×10^{9}	2.2×10^{15}	1.3×10^{9}	5.6×10^{8}	9.2×10^{8}	2.8×10^{42}	0.25	1.00	H	c
s15.40.1	40	7.72×10^{-14}	5.37×10^{9}	2.4×10^{15}	1.5×10^{9}	5.7×10^{8}	7.0×10^{8}	2.5×10^{42}	0.40	1.00	H, Na, Ca	
s15.43.1	43	1.01×10^{-13}	4.58×10^{9}	2.4×10^{15}	1.4×10^{9}	5.2×10^{8}	6.5×10^{8}	1.9×10^{42}	0.25	1.00	H	
s15.43.2	43	5.28×10^{-14}	4.08×10^{9}	2.7×10^{15}	1.4×10^{9}	5.2×10^{8}	7.2×10^{8}	2.5×10^{42}	0.25	1.00	H	
s15.43.3	43	1.10×10^{-13}	8.13×10^{9}	2.3×10^{15}	1.5×10^{9}	5.5×10^{8}	6.3×10^{8}	2.1×10^{42}	0.40	1.00	H, Ca, Fe	
s15.46.1	46	8.31×10^{-14}	4.76×10^{9}	2.6×10^{15}	1.4×10^{9}	4.8×10^{8}	6.5×10^{8}	2.5×10^{42}	0.25	1.00	H	
s15.46.2	46	7.40×10^{-14}	6.14×10^{9}	2.7×10^{15}	1.5×10^{9}	5.0×10^{8}	6.7×10^{8}	2.6×10^{42}	0.40	1.00	H, Ca, Fe	
s15.60.1	60	1.87×10^{-13}	8.78×10^{8}	1.8×10^{15}	1.4×10^{9}	1.8×10^{8}	3.4×10^{8}	6.4×10^{41}	0.25	1.00	H	
s15.60.2	60	6.26×10^{-14}	2.85×10^{9}	3.0×10^{15}	1.5×10^{9}	4.0×10^{8}	5.8×10^{8}	2.5×10^{42}	0.25	1.00	H	
s15.60.3	60	2.15×10^{-13}	5.09×10^{9}	1.8×10^{15}	1.3×10^{9}	2.5×10^{8}	3.6×10^{8}	1.0×10^{42}	0.40	1.00	H	
s15.60.4	60	9.38×10^{-14}	3.98×10^{9}	2.7×10^{15}	1.7×10^{9}	3.8×10^{8}	5.2×10^{8}	2.6×10^{42}	0.40	1.00	H, Na, Ca	
s25n2a models												
s25.5.1	5	3.72×10^{-12}	8.57×10^{11}	2.1×10^{14}	6.4×10^{8}	6.0×10^{8}	6.3×10^{8}	3.2×10^{42}	0.25	1.00	H, He	
s25.30.1	30	8.25×10^{-14}	2.79×10^{10}	1.5×10^{15}	7.1×10^{8}	4.8×10^{8}	5.8×10^{8}	2.1×10^{42}	0.25	1.00	H	
s25.60.1	60	6.82×10^{-14}	4.66×10^{9}	2.4×10^{15}	7.9×10^{8}	3.4×10^{8}	4.7×10^{8}	2.1×10^{42}	0.25	1.00	H	
10hmm models												
10h.30.1	30	1.38×10^{-12}	1.69×10^{10}	1.0×10^{15}	1.1×10^{9}	3.5×10^{8}	3.9×10^{8}	4.4×10^{41}	0.25	0.33	H	
10h.60.1	60	6.93×10^{-13}	6.95×10^{9}	1.44×10^{15}	8.0×10^{8}	2.3×10^{8}	2.8×10^{8}	7.0×10^{42}	0.25	0.33	H	
Exponential Atmospheres												
e12.1	11.6	2.18×10^{-13}	3.60×10^{10}	3.9×10^{14}	8.4×10^{8}	3.0×10^{8}	3.6×10^{8}	1.2×10^{41}	0.25	1.00	H	d
e12.2	11.6	3.95×10^{-13}	9.07×10^{10}	3.6×10^{14}	4.2×10^{9}	1.5×10^{9}	1.8×10^{9}	1.2×10^{41}	0.25	1.00	H	e
e12.3	11.6	6.7×10^{-14}	1.75×10^{10}	9.0×10^{14}	6.8×10^{8}	1.9×10^{9}	9.0×10^{8}	5.5×10^{41}	0.25	1.00	H	f

[a] Velocity scaled by 0.75
[b] Velocity scaled by 0.78
[c] Velocity scaled by 0.84
[d] In eqn (2.1), $\rho_0 = 1.7 \times 10^{-13}$ g cm^{-3}, $r_0 = 4 \times 10^{14}$ cm, and $dr_0 = 4.3 \times 10^{13}$ cm.
[e] Same as e12.1, but with velocity scaled by 5.0
[f] Similar to e12.1, but with $r_0 = 8.2 \times 10^{14}$ cm and $dr_0 = 9.6 \times 10^{13}$ cm.

As stated previously, we assume that all explosion models are expanding freely. The power-law atmospheres and exponential atmosphere are also homologous, meaning that the velocity v at radius r is given by $v = r/t$, where t is the elapsed time since explosion. For the KEPLER models s15s2a, s25n2a, and 10hmm, we assume that at Lagrangian mass coordinate $m = 4\pi \int_0^r r^2 \rho\, dr$, $r(m,\ t) = r(m,\ t_0) + v(m)(t - t_0)$, where t_0 is the time after explosion to which the model was hydrodynamically evolved with the KEPLER code.

The chemical abundances used in each calculation are indicated in columns (12) and (13) of Table 1 for the power-law models, and in columns (10) and (11) of Table 2 for the other models. The helium mass fractions, Y, was usually taken to be either 0.25 or 0.4., with 99% of the remaining gas being hydrogen, $X \approx 1 - Y$. All elements heavier than helium are grouped together as *metals*, and their abundances were taken to be solar, using values from Anders & Grevesse (1989). In calculations designed to study the effect of metallicity variation (models p6.60.3, p6.60.4, and s15.19.4), the abundance of all metals was multiplied by the same constant factor Z, which is given in columns (13) and (11) of Tables 1 and 2, respectively.

Figure 2 displays the range in total mass density at the photosphere, $\rho_{\rm ph}$, electron density at the photosphere, $N_{e,\rm ph}$, and effective temperature, $T_{\rm eff}$, covered by the models in Tables 1 and 2. Our grid of models does not sample either $T_{\rm eff}$ or ρ uniformly. Only a few of our models have effective temperatures greater than 10^4 K. Recombination wave atmospheres all cluster around $T_{\rm eff} \sim 5 \times 10^3$ K appropriate for recombination wave phase SNe II. The value of $\rho_{\rm ph}$ is approximately constrained by the observed rate of expansion and time since explosion. Assuming the density structure is a power law, we can write for the optical depth at the photosphere

$$\tau_{\rm ph} \approx \frac{\rho_{\rm ph}\sigma_e V_{\rm ph} t}{\mu_e(n-1)} = \frac{2}{3}. \tag{11}$$

Typical expansion velocities from spectra of photospheric phase SNe IIp are $V_{\rm ph} \sim 2 \times 10^3$ km s^{-1} to $\sim 1.5 \times 10^4$ km s^{-1}. With $V_{\rm ph}$ and an estimate of t, $\rho_{\rm ph}/(n-1)$ is given approximately by

$$\frac{\rho_{\rm ph}}{n-1} \sim 4 \times 10^{-15} \left(\frac{\mu_e}{m_{\rm H}}\right)\left(\frac{10^9 \text{ cm s}^{-1}}{V_{\rm ph}}\right)\left(\frac{5 \text{ days}}{t}\right) \text{g cm}^{-3}. \tag{12}$$

With three exceptions, the models in Tables 1 and 2 have $\rho_{\rm ph} \sim 10^{-14}$ to 3×10^{-13} g cm^{-3}, giving expansion velocities $V_{\rm ph} \sim 3 \times 10^3$ km s^{-1} to $\sim 1.2 \times 10^4$ km s^{-1} at times $5 \leq t \leq 60$ days.

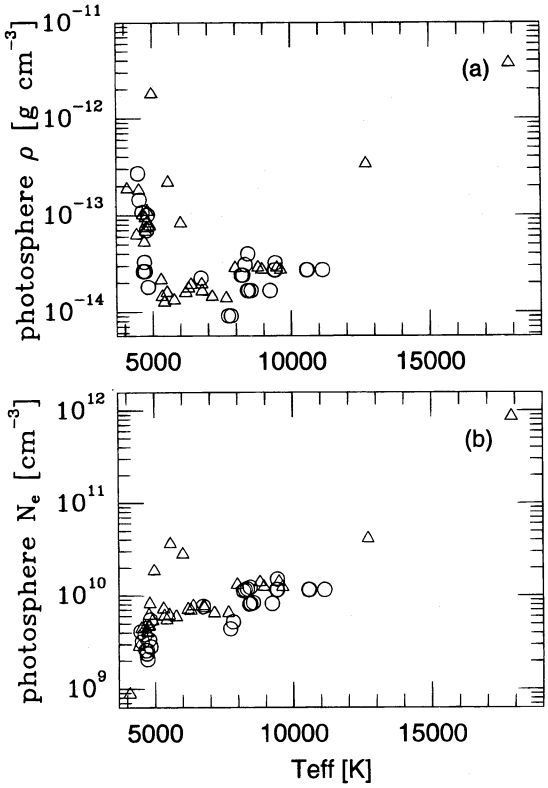

FIG. 2.—The range of photospheric densities and effective temperatures covered by models in this paper. (*a*): Mass density at $\tau_e = \frac{2}{3}$ vs. $T_{\rm eff}$ for power-law models (*circles*) and non–power-law models (*triangles*). (*b*): Photospheric electron density vs. $T_{\rm eff}$.

2.3. *Equation of State and Opacity Contributions*

The atmosphere calculations were performed with the non-LTE radiative transport code EDDINGTON (Eastman & Pinto 1993). Briefly, this code works as follows: using current estimates of level populations and gas temperatures, opacity and emissivity contributions are computed and used to solve a modified transport equation (§ 4) in the comoving frame. This formal solution gives the monochromatic radiation field mean intensity, J_ν, in the gas frame. An important by-product of the formal solution are the so-called *approximate lambda operators* (e.g., Kalkofen 1987) which, along with the J_ν, are used in the following step, which is solution of the equations of statistical equilibrium and thermal balance for new level populations and gas temperatures. Although the radiation field formal solution includes opacity and emissivity contributions from both lines and continua, bound-bound radiative rates appearing in the statistical equilibrium equations are evaluated accurately using the Sobolev approximation (Sobolev 1960). The basic iteration cycle—a radiation field formal solution followed by recalculation of level populations and gas temperature—proceeds until the largest relative change in any level population in any zone is less than 0.01. This is a more conservative convergence strategy than it appears because the last levels to converge are usually highly excited states with the smallest populations, so that when the model is judged to have converged for all states globally, the cycle to cycle change in temperature, luminosity or computed spectrum are $\ll 1\%$. Great care was also taken to ensure global energy balance, which is critical for computing accurate surface fluxes.

We model the photospheric layers and the overlying line-forming region. Densities there are high enough that the gas can be approximated as being in statistical and thermal equilibrium. The former implies that the rates into and out of a given state are equal, while the latter constrains the gas temperature by balancing the local rates of heating and cooling. The validity of these assumptions depends upon the electron density, N_e. Permittted radiative decay rates out of excited states, ranging from $\lesssim 1$ s^{-1} to $\gtrsim 10^9$ s^{-1}, are fast enough to ensure that the relative populations within an ionization stage are in equilibrium. The fastest rate at

which ionization can respond to changing conditions in gas density and radiation field is the recombination time, $t_{\rm rec} = (\alpha_{\rm rec} N_e)^{-1}$. For a typical recombination coefficient of $\alpha_{\rm rec} \sim 10^{-13}$ cm^3 s^{-1} and electron density of $N_e \sim 10^{10}$ cm^{-3}, $t_{\rm rec} \sim 10^3$ s which, at 10^6 s $\lesssim 10^7$ s, is much less than the timescale over which the density or radiation field evolve. Typical electron densities in the models of Tables 1 and 2 range from 10^{14} cm^{-3} in the high-density inner layers to 10^6 cm^{-3} in the fast, low-density and optically thin layers above the photosphere. In these latter regions, the computed temperature is probably an overestimate; however, the optical depths in these layers are small enough to have a negligible effect on the emergent spectrum. The electron density at the photosphere is always large enough that the uncertainty in the computed temperature which results from assuming thermal equilibrium is small. A rough estimate of this is

$$\delta T_u \approx \frac{\rho e_g}{t\, \partial H/\partial T}\,, \tag{13}$$

where e_g is the gas specific energy, $\partial H/\partial T$ is the temperature derivative of the net heating rate, and t is the elapsed time since explosion. In our models, we always have $\delta T_u \lesssim 1$ K at the photosphere and in regions in which the hydrogen Balmer lines form (see § 1 and Figs. 5 and 6).

In each calculation, the excitation and ionization of select elements was assumed to depart from a Saha-Boltzmann distribution and was computed explicitly (treated non-LTE). Columns (14) of Table 1 and column (12) of Table 2 summarize the non-LTE ions employed for each model. Since all chemical compositions were hydrogen dominated, H and H$^-$ were always treated non-LTE. In several calculations, we also computed the non-LTE excitation and ionization of He I–III, Ca I–III, Na I–II, and Fe I–III.

Absorptive opacity contributions included all bound-free, free-free, and bound-bound transitions for the elements explicitly included in the atomic model, as well as H$^-$ bound-free and H I Lyα Rayleigh scattering, and electron scattering.

For elements other than the ones listed in Tables 1 and 2, the excitation and ionization were assumed to be given by the Saha-Boltzmann equation. These *metals* have an opacity contribution which was approximated as complete scattering. For the low densities encountered in SNe II photospheres, pure scattering is consistent with the fact that collisional depopulation of an excited upper level is much less likely that radiative de-excitation. An estimate of the electron collisional de-excitation probability, due to Anderson (1989), and based on the approximate collision cross section formula of Van Regemorter (1962), is

$$\delta = \frac{C_{\rm ul}}{C_{\rm ul} + A_{\rm ul}} \approx \frac{N_e}{N_e + q(h\nu/1\ {\rm eV})^3}\,, \tag{14}$$

where $A_{\rm ul}$ and $C_{\rm ul}$ are the radiative and collisional de-excitation rates, respectively. For iron, Anderson finds $q \sim 10^{13}$–10^{14} cm^{-3}. Consequently, for $N_e \ll 10^{14}$ cm^{-3}, as is generally the case in SNe II photospheres, it is much more accurate to assume pure scattering than pure absorption for transitions at $\lambda < 4000$ Å. However, the branching ratio for emitting a photon of the same energy as the one absorbed may be less than unity, an effect which gives rise to photon splitting (Pinto 1988; Xu 1989; Li & McCray 1996). This effect, along with departures from LTE, are unlikely to be serious sources of error in our calculations. This is because the most important contribution from metal lines is to the UV opacity, which is so great that, in the recombination phase of the light curve, little energy comes out shortward of 4000 Å, which means that large variations in metallicity or moderate numerical corrections to the UV opacity have only a modest effect on either the temperature structure or the optical continuum. Metallicity effects on the optical continuum are discussed in § 3. The line opacity from *metals* was computed from a list of approximately 200,000 transitions taken from the compilation of Kurucz (1991). The opacity was approximated probabilistically as an "expansion opacity," as described in Eastman & Pinto (1993). In this approximation, the opacity contribution from lines in a frequency interval $(\nu, \nu + \Delta\nu)$ is given by

$$k_{\rm exp} = \frac{\nu}{\Delta\nu}\frac{v}{rc}\sum_j \int_0^1 (1 + Q\mu^2)\{1 - \exp\,[-\tau_j(\mu)]\}d\mu\,, \tag{15}$$

where the sum is over all lines in the interval $(\nu, \nu + \Delta\nu)$, $Q \equiv d\ln v/d\ln r - 1 \approx 0$, and $\tau_j(\mu) = (h/4\pi)(n_l B_{ll'} - n_{l'} B_{l'l})/[(\partial v/\partial r)(1 + Q\mu^2)/c]$ is the Sobolev optical depth of line j linking levels l and l', with level populations, n_l, and Einstein B-coefficients $B_{ll'}$. Also, μ is the cosine of the angle between the direction of propagation and the local radius vector. Eastman & Pinto (1993) argued that, for typical supernova conditions, the time a photon spends while in resonance with a line is much less than the time spent between resonances. Consequently, the entire process of a photon going into resonance with a line, being absorbed, scattering in the line and finally being reemitted on the long-wavelength side of the line in a new direction, can be treated as a single scattering event. That is the essence of equation (15). The effective opacity from lines in an interval $(\nu, \nu + \Delta\nu)$ is the average number of line interactions undergone while Doppler shifting through $\Delta\nu$, divided by the distance $\sim ct\,\Delta\nu/\nu$. The main shortcoming in this approximation is that, as we have said, it does not take into account branching. We do not consider this to be an important issue for plateau phase SNe IIp, for reasons which are discussed in § 4.

2.4. *Radiation Transport*

The radiation field is *not* in equilibrium, at least not in the sense that is usually applied to nonvariable stars in which conditions change little over a Kelvin-Helmholtz time. Type II supernovae are expanding and cooling. However, they do so in a way which, in the photospheric layers, allows the fully time-dependent transport equation to be reduced to a much simpler transfer equation, with boundary conditions given by only one parameter: the bolometric luminosity in the gas frame.

To first order in $\beta = v/c$, the comoving frame equation of radiative transport in spherical geometry may be written (see, e.g., Mihalas 1978, pp. 490–502)

$$\frac{1}{c}\frac{DI_\nu}{Dt} + \mu\frac{\partial I_\nu}{\partial r} + \frac{1-\mu^2}{r}(1 - \beta Q\mu)\frac{\partial I_\nu}{\partial \mu} + \frac{\beta}{r}\left(3 - \frac{\partial}{\partial \ln \nu}\right) \times (1 + Q\mu^2)I_\nu = -\chi_\nu I_\nu + \sigma_\nu J_\nu + \eta_\nu\,, \tag{16}$$

where $DI_\nu/Dt \equiv \partial I_\nu/\partial r + v\,\partial I_\nu/\partial r$; $Q \equiv d\ln\beta/d\ln r - 1$; σ_ν is the monochromatic (and by the usual assumption, isotropic) scattering opacity; $\chi_\nu = \sigma_\nu + k_\nu$ is the total monochromatic opacity, including both scattering and true absorption; $J_\nu = \frac{1}{2}\int_{-1}^{1} I_\nu\, d\mu$ is the angle averaged mean

intensity, and η_ν is the emissivity. For homologous expansion, $\partial\beta/\partial r = 1/ct$ and $Q = 0$. The fully relativistic form is derived by Castor (1972). Since the highest velocity considered in this paper or encountered in supernova spectra is 3×10^9 cm s^{-1}, the Lorentz factor $1/(1-\beta^2)^{1/2} < 1.005$ and may safely be set equal to unity, and terms of $O(\beta^2)$ and higher may be dropped, as was done in equation (16).

Integrating equation (16) over angle and frequency, and assuming radiative equilibrium, the result can be written

$$\frac{DE}{Dt} = \frac{1}{4\pi r^2}\frac{\partial L}{\partial r} - Q\frac{v}{r}P - \frac{v}{r}(4-Q)E\,, \qquad (17)$$

where E is radiation field energy density, P is the radiation pressure, L is the bolometric luminosity, and all quantities are as measured in the gas frame. If the expansion is homologous such that $Q \approx 0$ and $v/r \approx 1/t$, this expression for DE/Dt becomes even simpler:

$$\frac{DE}{Dt} = \frac{1}{4\pi r^2}\frac{\partial L}{\partial r} - \frac{4E}{t}\,. \qquad (18)$$

During both the initial diffusive cooling phase and the recombination phase which follows it, the luminosity is powered by shock deposited energy diffusing out from a depth $\tau_{\rm diff}$. For a power-law atmosphere of the form $\rho = \rho_0 r^{-n} t^{n-3}$ and with an initially uniform temperature distribution and constant opacity coefficient, κ, the optical depth of the diffusion wave is given by

$$\tau_{\rm diff} = \frac{\eta_c}{n-1}\left(\frac{3\kappa\rho_0}{c}\right)^{-[(n-1)/(n-2)]}\kappa\rho_0 t^{2/(n-2)} \qquad (19)$$

(Chevalier 1992), and it is in this region that $\partial L/\partial r$ deviates appreciably from zero. Here η_c is a constant of order unity. At smaller optical depths, $L \approx$ constant. At greater depths and in the absence of radioactive heating, $L \approx 0$. This result follows from the analytic solution of the diffusion equation in a homologously expanding power-law density atmosphere (Chevalier 1992) and from numerical studies (e.g., EWWP). During the recombination phase the luminosity emanates from an optical depth $\tau_{\rm rw}$, given by

$$\tau_{\rm rw} \approx \frac{4}{3}\left(\frac{T_{\rm int}}{T_{\rm eff}}\right)^4\,, \qquad (20)$$

where $T_{\rm int}$ is the temperature internal to the recombination front. Figure 3 shows the variation with time and gas velocity of the comoving frame bolometric luminosity in the 15 $M_\odot$ RSG explosion studied by EWWP with a multigroup radiation transport code. This calculation made no assumptions about how L varies with depth; the fully time-dependent radiation transport problem was solved. This figure shows that through the photosphere and above it, the comoving frame luminosity is very close to being constant. For comparison, the observer frame light curve and effective temperature evolution for this model are reproduced in Figure 4.

Since $\partial L/\partial r \approx 0$, it follows that

$$\frac{DE}{Dt} \approx \frac{4E}{t}\,, \qquad (21)$$

and the radiation field evolves as a $\gamma = 4/3$ gas undergoing adiabatic decompression. The D/Dt term is of the same size and opposite sign as all the other velocity terms in equation (16) combined, and substantial error in the surface bolometric luminosity could arise if this term is neglected. Specifically, if an amount of energy per second L_0 is put in at the lower boundary of an atmosphere in thermal equilibrium, then the amount of energy coming through the photosphere will be less than L_0 by an amount

$$\frac{\Delta L}{L} = 1 - \exp\left(-\frac{4l}{ct}\right) \approx 1 - \exp\left(-\frac{12\tau\,\Delta v}{c}\right)\,, \qquad (22)$$

where l is the total path length which photons take in diffusing from the lower boundary at optical depth τ to the photosphere, and Δv is the velocity difference. As a realistic example, suppose $\tau = 20$ and $\Delta v = 10^8$ cm s^{-1}. Then $\Delta L/L = 0.55$, which in the context of EPM is unacceptably large.

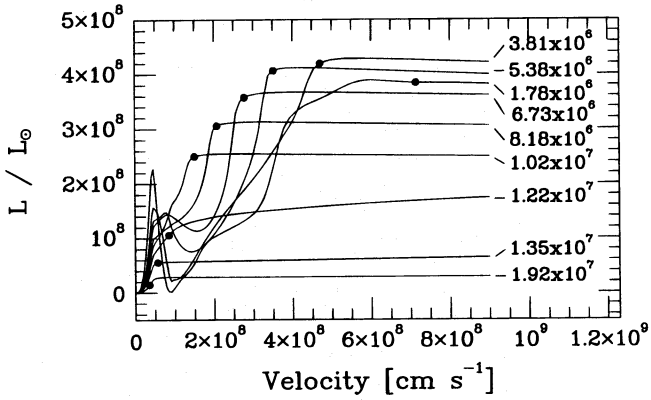

FIG. 3.—Evolution of the gas frame bolometric luminosity as a function of expansion velocity for model s15s7b (Eastman et al. 1994). Each curve is labeled by the time after explosion in seconds. The points mark the position of the photosphere. This figure shows that, in an SN IIp during the plateau phase, it is a good approximation to assume constant comoving frame bolometric luminosity through the photosphere. In this example, the assumption is worse around 1.22×10^7 s because transparency has set in and the luminosity is dropping rapidly as the light curve goes from plateau to tail (see Fig. 4).

The generalization of equation (21) for a nonhomologous velocity field and nonisotropic radiation field (eq. [16]) is

$$\frac{1}{c}\frac{DI_\nu}{Dt} \approx Q\frac{B}{r}(\mu-\mu^3)\frac{\partial I_\nu}{\partial\mu} - 4\frac{\beta}{r}(1+Q\mu^2)I_\nu\,. \qquad (23)$$

Using this expression for DI_ν/Dt, the transport equation, (16), becomes a much simpler transfer equation:

$$\mu\frac{\partial I_\nu}{\partial r} + \frac{1-\mu^2}{r}\frac{\partial I_\nu}{\partial\mu} - \frac{\beta}{r}\left(1+\frac{\partial}{\partial\ln\nu}\right) \times (1+Q\mu^2)I_\nu = -\chi_\nu I_\nu + \sigma_\nu J_\nu + \eta_\nu\,. \qquad (24)$$

It is straightforward to show that when the gas is in radiative equilibrium [$4\pi\int_0^\infty (k_\nu J_\nu - \eta_\nu)d\nu = 0$], this modified transfer equation gives $L = L_{\rm bol}$ = constant.

In equation (24), photons travel along straight-line trajectories, and this, combined with the assumption of isotropic scattering, lets one derive equivalent equations to equation (24) for the Feutrier variables $u_\nu \equiv [I_\nu(\mu) + I_\nu(-\mu)]/2$ and $v_\nu \equiv [I_\nu(\mu) - I_\nu(-\mu)]/2$, and moment equations for J_ν and $H_\nu \equiv \int_{-1}^{1} I_\nu(\mu)\mu\,d\mu$. These equations are solved by a finite difference technique similar to that described by Mihalas, Kunasz, & Hummer (1976), on a frequency grid of 2000–5000 variably spaced points ranging from 50 Å to 600 μm. All calculations employed 50 depth zones, and spacing was logarithmic in the column density. Note that, since photon

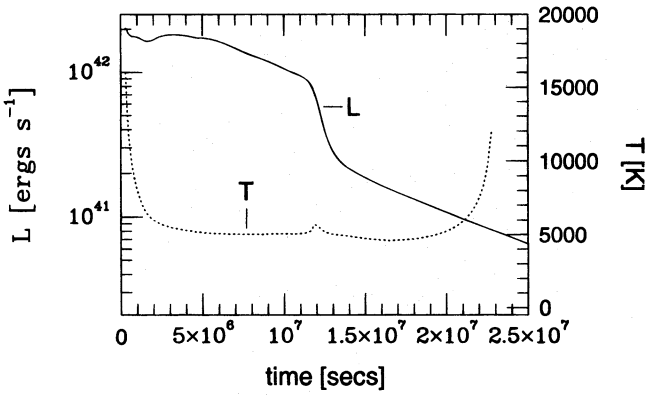

FIG. 4.—Bolometric light-curve and effective temperature evolution of the 15 $M_\odot$ explosion model s15s7b (Eastman et al. 1994), which is similar to the 15 $M_\odot$ explosion model s15s2a considered in this paper.

trajectories are linear, the effects of relativistic aberration, which is proportional to Q, vanish.

As in stellar atmosphere calculations, the lower boundary condition is formulated as a diffusion boundary condition: the flux at the lower boundary is given by

$$\mathscr{F}_\nu = \frac{L_{\rm bol}}{4\pi r_{3/2}^2}\frac{h_\nu}{\int_0^\infty h_{\nu'}\,d\nu'}, \tag{25}$$

where $L_{\rm bol}$ is the bolometric luminosity in the gas frame, $r_{3/2}$ is the radius of the middle of the innermost zone, and

$$h_\nu = -\frac{4\pi}{3}\frac{\partial T}{\partial r}\nu^{-1}\int_\nu^\infty \frac{\partial B_{\nu'}}{\partial T} R_{\rm H}\left(\frac{\nu'}{\nu}\right)^{[(R_{\rm H}/R_{\rm V})-1]} \times \exp\left(-R_{\rm H}\int_\nu^{\nu'}\frac{\chi_{\nu'}}{\nu''}\,d\nu''\right)d\nu' \tag{26}$$

is the diffusion limit flux in the comoving frame. Here $R_{\rm H} \equiv 5/(3\,\partial\beta/\partial r + 2\beta/r)$ and $R_{\rm V} \equiv (\partial\beta/\partial r)^{-1}$. The bolometric luminosity used in each model is given in column (11) of Table 1 for the power-law atmospheres, and in column (9) of Table 2 for the KEPLER and exponential atmosphere models.

The outer boundary was chosen to be at a position in the gas which was moving faster than the highest velocity feature in observed SNe IIp spectra, typically 15,000–20,000 km s^{-1}. The velocity of the outer boundary, $V_{\rm max}$, is given in columns (8) and (6) of Tables 1 and 2, respectively. The inner boundary was chosen to correspond to an electron scattering optical depth of $\tau_e \sim 20$. The diffusion boundary condition, equation (25), is only an accurate description of the radiation field at the innermost zone when that zone is placed deep enough inside the atmosphere that gas and radiation field are thermalized. In the absence of significant nonthermal heating, the depth at which gas and the radiation field come into thermal equilibrium, the *thermalization depth*, or $\tau_{\rm thm}$, was approximated roughly in equation (6), but it is given more accurately by the condition

$$\int_0^{\tau_{\rm thm}(\nu)}\sqrt{\frac{3k_\nu}{k_\nu+\sigma_\nu}}\,d\tau_\nu = 1 \tag{27}$$

(Wagoner 1982). The role that $\tau_{\rm thm}(\nu)$ plays in determining the color temperature of the emergent flux at the photosphere was discussed in § 1. When the lower boundary has been placed deep enough in the atmosphere, the atomic level populations go to a Saha-Boltzmann distribution, and the radiation field mean intensity approaches a Planck function at the local gas temperature. Failure to ensure thermalization can introduce artifacts into the transfer solution. We have found that $\tau_{\rm thm} \sim 1$–5, and that $\tau_e = 20$ is sufficiently deep.

3. TYPE II SUPERNOVA ATMOSPHERE MODELS AND PARAMETER SENSITIVITIES

In this section we discuss the atmosphere solutions, describe the appearance of model spectra, and explore the way parameters of our model atmospheres influence the emergent observer frame spectrum.

3.1. *Temperature and Ionization Structure*

Corresponding to the two phases of photospheric evolution described at the beginning of § 2, there are two basic prototypes for the ionization and thermal structure of a hydrogen-dominated Type II supernova atmosphere, the main difference between them being the effective temperature, $T_{\rm eff}$. If $T_{\rm eff} \gg 5000$ K, most of the hydrogen above the photosphere is ionized, and possibly the helium as well. Once $T_{\rm eff}$ approaches 5000 K, hydrogen begins recombining, and the photosphere is determined by the position of the inward-moving recombination front. Subsequently, $T_{\rm eff}$ stays near 5000 K until after the end of the plateau. As discussed in EWWP, the computed value of $T_{\rm eff}$ during the recombination phase is sensitive, to a certain extent, to how the opacity is treated, particularly the contribution from UV line blanketing, which lowers $T_{\rm eff}$. In light-curve calculations, failure to account for the line blanketing effect of UV absorbers will result in the computed $T_{\rm eff}$ being too high and the plateau duration too short.

The examples shown in Figures 5 and 6 typify both phases. Figure 5 shows the computed gas temperature and ionization, $X_e \equiv N_e/N_{\rm nuc}$, where N_e and $N_{\rm nuc}$ are the number density of free electrons and of nuclei, respectively, for model p12.10.9, which has an effective temperature $T_{\rm eff} = 10{,}585$ K. In this model, H and He are completely ionized everywhere. The position of the electron scattering photosphere thus depends only on the instantaneous dis-

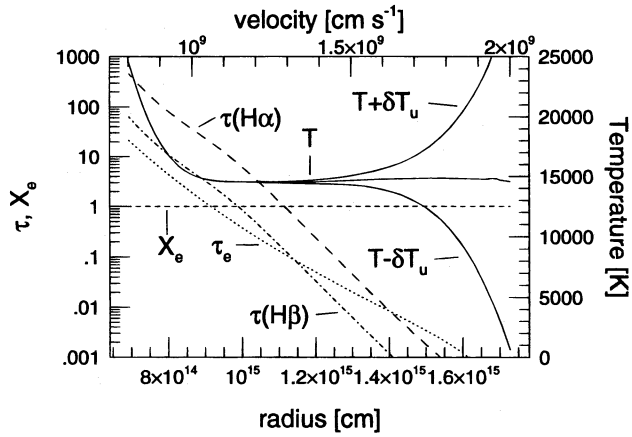

FIG. 5.—Temperature solution and ionization index ($X_e \equiv N_e/N_{\rm nuc}$) for a typical "hot" atmosphere, model p12.10.9 ($T_{\rm eff} = 10{,}585$ K). H and He are completely ionized in this model, and $X_e \sim 1$ everywhere. Also shown are the electron scattering optical depth (τ_e) and the Sobolev optical depths for the Hα [τ(Hα)] and Hβ [τ(Hβ)] transitions. The two curves labeled $T + \delta T_u$ and $T - \delta T_u$ show the range of uncertainty in the computed temperature, as defined by eq. (13).

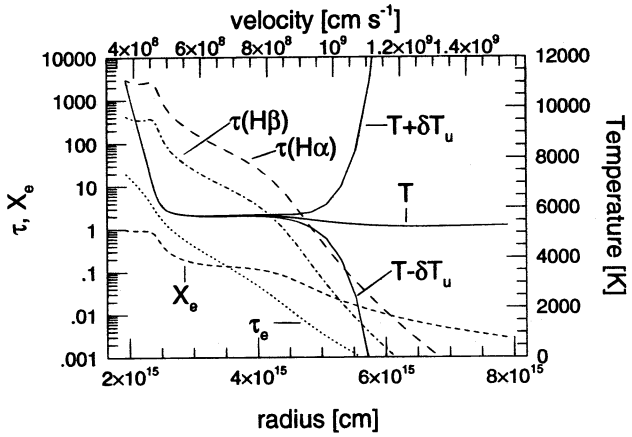

FIG. 6.—Temperature solution and ionization index in a typical "cool" atmosphere, model p6.60.1 ($T_{\rm eff} = 4.658$ K). He is essentially neutral exterior to $\tau_e \sim 20$, and the photosphere forms at the H recombination front, where $X_e \equiv N_e/N_{\rm nuc}$ drops below 1. A region of partial ionization extends for some distance above the photosphere, at which recombinations populate the $n = 2$ level of H and cause the Balmer lines to remain optically thick far above the photosphere. As in Fig. 5, the two curves labeled $T + \delta T_u$ and $T - \delta T_u$ show the range of uncertainty in the computed temperature, as defined by eq. (13).

tribution of mass with radius. The gas temperature above the photosphere is always greater than the effective temperature, as was shown by Yakeda (1990, 1991). This is because, as already discussed, the continuum opacity is dominated by electron scattering, which causes the radiation field emergent from the photosphere to have a higher color temperature, T_c, than $T_{\rm eff}$. The emergent flux resembles a Planck function established at the gas temperature of the thermalization depth, $\tau_{\rm thm}(\nu)$ (eq. [27]), but diluted by an amount $\sim 1/\tau_{\rm thm}(\nu)$. Above the photosphere, the gas temperature is set by the color temperature of the continuum radiation field. Also shown is the range of temperature uncertainty, $T \pm \delta T_u$ (eq. [13]) which results from assuming radiative equilibrium. In this model, T is well determined for $v \lesssim 1.5 \times 10^9$ cm s^{-1}, which is outside the region in which H Balmer lines make a substantial contribution to the emergent spectrum.

Figure 5 also shows the electron scattering optical depth and Sobolev optical depths for the H I Hα and Hβ transition. Both Hα and Hβ arise from the same lower level, the $n = 2$ state of hydrogen, so the Hβ optical depth follows that of Hα but is shifted down by 0.14. Because Hβ is weaker and does not extend as far out as Hα, the blueshift velocity of its absorption trough will be closer to that of the photosphere. As the photosphere recedes and cools, Hβ and the higher order members of the Balmer series become subject to contamination from Fe II and Ti II transitions, which broaden the absorption trough. As a rule of thumb, the blueshift velocity of unblended transitions decreases with decreasing line strength, which is important for determining the photospheric expansion rate from spectra.

Figure 6 shows the gas temperature and ionization fraction for a typical "cool" atmosphere, model p6.60.1, which is a power-law atmosphere with $n = 6$ and $T_{\rm eff} = 4658$ K. The photosphere is at a point at which the gas is only partially ionized. The run of ionization with radius or velocity does not fall off rapidly above the photosphere. Rather, there is a region in which $X_e \sim 0.1$–0.2, extending in radius up to $\sim 1.5 R_{\rm ph}$. In this extended, partially ionized region, recombination is very effective at populating the $n = 2$ level of hydrogen, and the Sobolev optical depths of the Balmer lines remain significant out to $\sim 2R_{\rm ph}$. A consequence of this partially ionized gas is that blueshift velocities derived from P Cygni absorption minima, V_m, will exceed the velocity of the photosphere, $V_{\rm ph}$, and if used as a measure of $V_{\rm ph}$, they can be a substantial overestimate. Note also that the computed temperature becomes uncertain above $v \approx 9 \times 10^8$ cm s^{-1} where the electron density is low, which, because $\tau(\rm H\alpha) \sim 1$, may affect the blue wing of the computed line profile. Clearly, deriving the photospheric velocity from Hα in supernovae at this stage of their evolution is fraught with difficulties, and it is best done with the weaker Balmer lines and metal lines.

3.2. *Example Spectra*

The most prominent spectroscopic changes which take place between shock breakout and the end of the plateau are due to cooling of the photosphere. These changes are exemplified by the spectra shown in Figures 7 and 8, which show, respectively, an effective temperature sequence of s15s2a models and of power-law atmospheres. The temperature drops rapidly during the first 2 weeks after explosion (e.g., Fig. 4), and spectral evolution is most rapid in the ultraviolet. Longward of the Lyman edge at 900 Å, absorption features start appearing at ~ 1.2–1.5×10^4 K. The strongest lines are those of the iron peak, especially Fe III and Ni III but also C II, O III, and Mg II. The only lines present in the optical, $\lambda > 4000$ Å, are the H I Balmer lines and He I λ5876. At $T_{\rm eff} \sim 8 \times 10^3$ K, the UV Fe III lines start to be replaced by lines of Fe II, the Balmer lines become stronger in the optical, and evidence of He I disap-

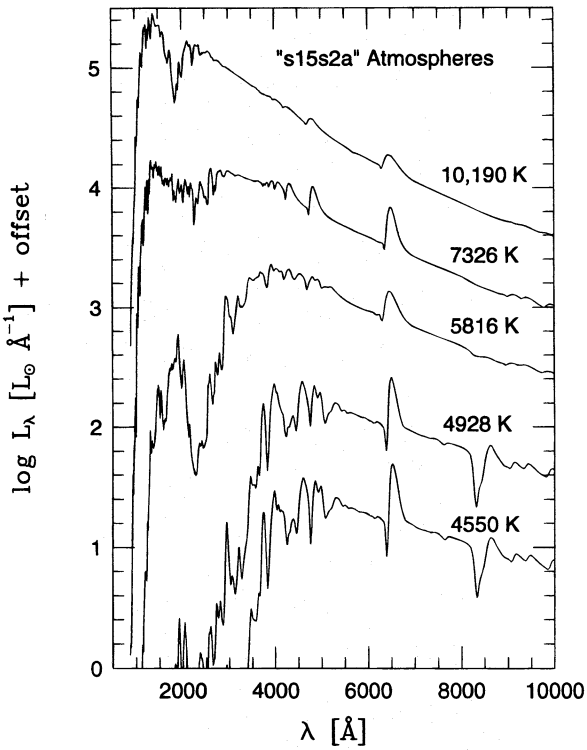

FIG. 7.—Computed spectra of various s15s2a atmosphere models, labeled by effective temperature. Shown are, from hottest to coolest, models s15.12.5, s15.19.5, s15.28.2, s15.46.1, and s15.60.2, which are described in Table 2.

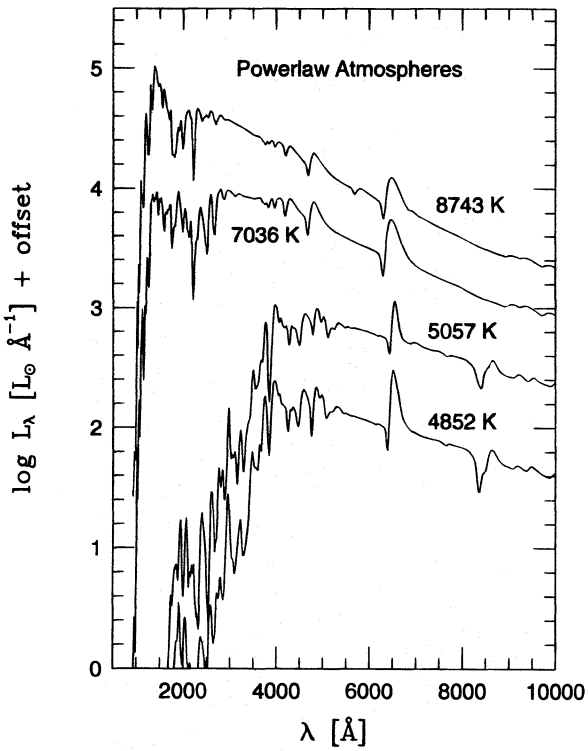

FIG. 8.—Computed spectra of various power-law density models, labeled by effective temperature. Shown are, from hottest to coolest, models p12.10.10, p12.10.4, p12.60.1, and p6.60.2, which are described in Table 1.

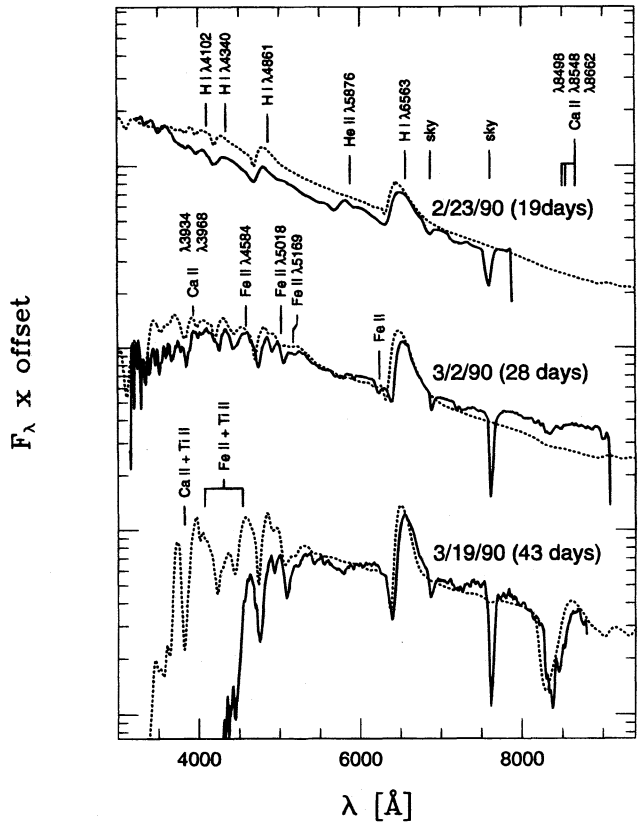

FIG. 9.—Comparison of model spectra and observations of the SN IIp 1990E. Observations are presented as solid curves, and each observation is labeled by date of observation and an estimate of the corresponding age after explosion. The dashed curves are spectra computed for the three models s15.19.3 (*top*), s15.28.2 (*middle*), and s15.43.2 (*bottom*).

pears. At still lower temperatures, the UV is heavily blanketed by lines of once ionized iron peak elements, Fe II and Ti II, and almost all the flux is carried at wavelengths longward of 4000 Å. The strongest lines in the optical and near-infrared, besides the Balmer lines, are the Ca II H and K lines at 3968 and 3934 Å and the Ca II infrared triplet lines at 8662, 8542, and 8498 Å. In the *B* band, from ~4000 to ~5000 Å, numerous lines of Fe II and Ti II appear which grow in strength as the photosphere recedes inward in Lagrangian mass coordinate, even though $T_{\rm eff}$ remains roughly constant at ~4500–5000 K. Although it is not present in any of the spectra shown in Figures 7 or 8, the Na I D line at 5890 Å is also observed to appear in SN IIp spectra during the middle of the plateau and to grow in intensity as the photosphere recedes. It is a strong resonance line, but most sodium is once ionized, and the ionization fraction of Na I does not become significant until the UV has been quenched enough to lower the line-forming region temperature, allowing there to be a significant Na I ionization fraction.

Figure 9 shows a comparison between 90E spectral observations and three atmospheres based on the KEPLER explosion model s15s2a. SN 1990E was discovered at maximum brightness on 1990 February 15 by the Berkeley Automated Supernova Search (Pennypacker et al. 1990; Schmidt et al. 1993a) and has been estimated to have exploded on or about 1990 February 4 (Schmidt et al. 1992). It was not present at a limiting magnitude of $m_v = 19$ on an image taken 1990 February 10, consistent with the 15 $M_\odot$ model of EWWP which does not reach visual maximum until 20 days after explosion. Both qualitatively and quantitatively, the resemblance between the models and observations is good, although the observed spectra were taken through various large amounts of terrestrial extinction, under nonphotometric conditions.

3.3. *Effect of* $d \ln \rho / d \ln r$ *Variation*

Figure 10 shows spectra of three power-law models which are otherwise nearly identical except that the density index, $n = -d \ln \rho / d \ln r$, has been changed. In each case the density constant (ρ_{15} in Table 1) was varied at the same time as n so as to yield a photospheric radius which is constant at $\sim 2.4 \times 10^{15}$ cm. Models p9.60.1 and p12.60.1 have a total bolometric luminosity of 2.2×10^{42} ergs s^{-1} and photospheric radii of 2.4×10^{15} cm and 2.3×10^{15} cm, respectively, while p6.60.1, because of its slightly higher luminosity at 2.7×10^{42} ergs s^{-1}, has a photospheric radius of 2.8×10^{15} cm. Because hydrogen is recombining at the photosphere, the effective temperature in all three models is nearly the same at 4758 K for p6.60.1, 4791 K for p9.60.1, and 4819 K for p12.60.1.

Despite the very different density indices of these three atmospheres, their continuum spectra are, both qualitatively and quantitatively, nearly identical. We attribute this to the fact that the effective temperatures are so similar. The main spectral differences are in the amount of energy emitted in the emission component of the Balmer lines, and in the blueshift velocity of P Cygni absorption troughs. Figure 11 shows the details of the Hα profiles for the three spectra plotted in Figure 10. As the density gradient is steepened, the equivalent width of the P Cygni emission

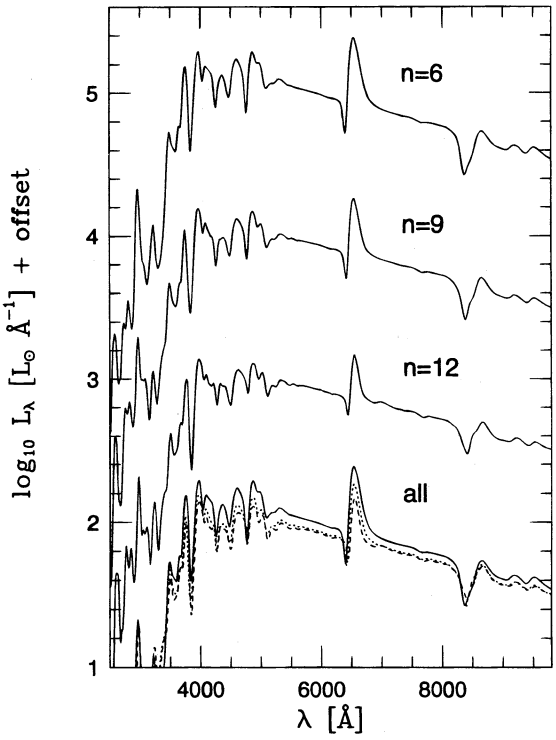

FIG. 10.—The effect of varying the density parameter $n \equiv -d \ln \rho / d \ln r$ is shown in this figure, which compares spectra of the power-law models p6.60.1 ($n = 6$ [*top, and solid curve on bottom*]), p9.60.1 ($n = 9$ [*second from top, and dotted curve on bottom*]) and p12.60.1 ($n = 12$ *third from top, and dashed curve on bottom*]). The spectra have been offset downward from each other in intervals of 1 dex. All three cases are shown together so that they may be compared more readily.

component goes down, and the blueshift velocity of the absorption trough decreases because there is less absorption by high-velocity gas. There is less emission because the Balmer line emission comes from the extended region of partial ionization above the photosphere, seen in Figure 6. In this partial ionization region, sufficient population in the $n = 2$ and 3 levels of hydrogen is maintained to reprocess continuum radiation by photoionization, followed by recombination, which gives the Balmer line emission. Steepening the density gradient decreases the amount of gas above the photosphere and diminishes the amount of continuum reprocessing which takes place.

Aside from its effect on the shape of line features, we do not expect the steepness to have a large direct effect on the thermal structure of the atmosphere. To understand why this is so, consider a power-law atmosphere, with density given by

$$\rho(r) = \rho_{\rm ph}\left(\frac{r}{R_{\rm ph}}\right)^{-n}, \tag{28}$$

where $\rho_{\rm ph}$ is the density at the photosphere ($\tau = \frac{2}{3}$), which is at radius $R_{\rm ph}$. If the mass opacity is constant with depth, which certainly is not the case at a recombination front, then in terms of optical depth τ, the density is

$$\rho = \rho_{\rm ph}\left(\frac{3\tau}{2}\right)^{n/(n-1)}, \tag{29}$$

and in the limit that $n \to \infty$.

$$\rho(\tau) \approx \rho_{\rm ph}\frac{3\tau}{2}\left[1 + \frac{1}{n}\ln\left(\frac{3\tau}{2}\right)\right]. \tag{30}$$

For large n, ρ is linear in τ and independent of n. Steepness has a modest effect on the thermal structure by altering the influence of spherical extension. In a spherically symmetric, constant luminosity atmosphere, the temperature distribution is not very different from that of a gray opacity atmosphere, and it goes as

$$T^4 \propto T_{\rm eff}^4\left(\frac{R_{\rm ph}}{r}\right)^2 \tau . \tag{31}$$

For $n \gg 1$, we can set $(R_{\rm ph}/r)^2 \approx 1$, which is the plane-parallel limit. At modest optical depths ($\tau \lesssim 20$), the variation in ρ with n is much smaller than its variation with $\rho_{\rm ph}$ and τ, and ρ can be regarded as being primarily a function of τ and $\rho_{\rm ph}$. This means that the main factors affecting the emergent flux and the flux dilution (§ 4) will be $T_{\rm eff}$ and $\rho_{\rm ph}$.

As the density in the atmosphere increases, true absorption increasingly dominates over electron scattering as the primary opacity mechanism, which has the effect of bringing gas and radiation field at the photosphere nearer to equilibrium, and the emergent flux closer to a Planck function at the effective temperature.

Figure 12 displays the spectra of models s15.5.1 and s25.5.1. In both these models, the photosphere forms in the very outermost, high-velocity gas in which the density distribution is represented accurately by a power law. In model s15.5.1, $-d \ln \rho / d \ln r \equiv n \approx 26$ and $T_{\rm eff} = 12{,}711$ K, and in model s25.5.1, $n \approx 88$ and $T_{\rm eff} = 17{,}875$ K. These two models might correspond to two points in the early evolution of an SN II: as the photosphere moves inward into gas of shallower density gradient, the effective temperature also drops. In model s25.5.1, hydrogen is highly ionized, and the Balmer lines are very weak. In both models, the Balmer lines extend to $\lambda = \lambda_0(1 - V_{\rm ph}/c)$ on the blue side of line center, where λ_0 is the line rest wavelength and $V_{\rm ph}$ is the photosphere velocity. On the long-wavelength side of line center, the line extends much further to the red than $\lambda = \lambda_0(1 + V_{\rm ph}/c)$, and the line emission peak joins the continuum only slowly. This is the result of line photons which have undergone multiple electron scatterings before escape. The effect of the gas density on the continuum flux dilution will be discussed in § 4.

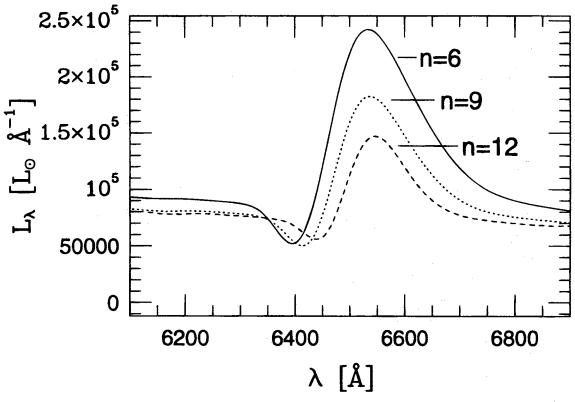

FIG. 11.—Details of the hydrogen Hα profile from the spectra shown in Fig. 9.

3.4. *Effects of Metallicity Variation*

Most of the opacity contributed by elements heavier than helium, especially the iron peak, is in the ultraviolet

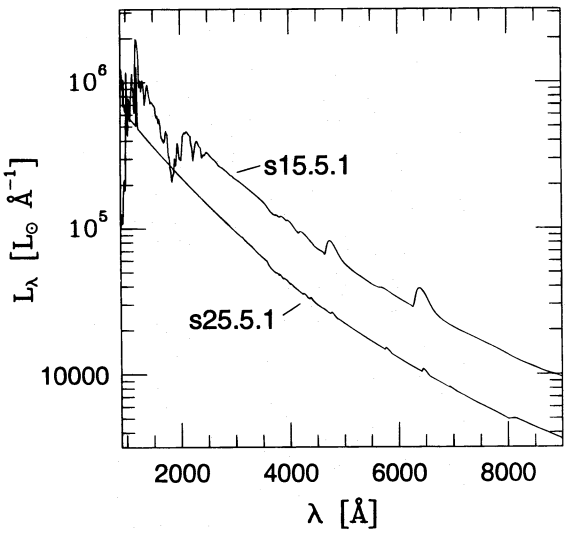

FIG. 12.—Spectra of two models which are represented accurately as large density gradient power laws: model s15.5.1, with $-d\ln\rho/d\ln r \equiv n \approx 26$ and $T_{\rm eff} = 12{,}711$ K and model s25.5.1, with $n \approx 88$ and $T_{\rm eff} = 17{,}875$ K.

($\lambda < 4000$ Å), although it is also important in the *B* band. The opacity from lines in the UV is so great during the recombination phase that the UV is saturated and very little energy emerges shortward of 4000 Å. This effect is demonstrated in Figure 13, where we have plotted spectra of models p6.60.1 ($Z = 1$, $T_{\rm eff} = 4658$ K), p6.60.3 ($Z = 0.3$, $T_{\rm eff} = 4732$ K), and p.6.60.4 ($Z = 3$, $T_{\rm eff} = 4706$ K). While a factor of 3 metallicity variation causes an almost equal factor of 3 variation in the far UV flux, there are only modest differences in the optical and IR continua, the spectral regions in which EPM is applied. There is a change in the strength of *B*-band Fe II and Ti II lines, but here the effect is also modest.

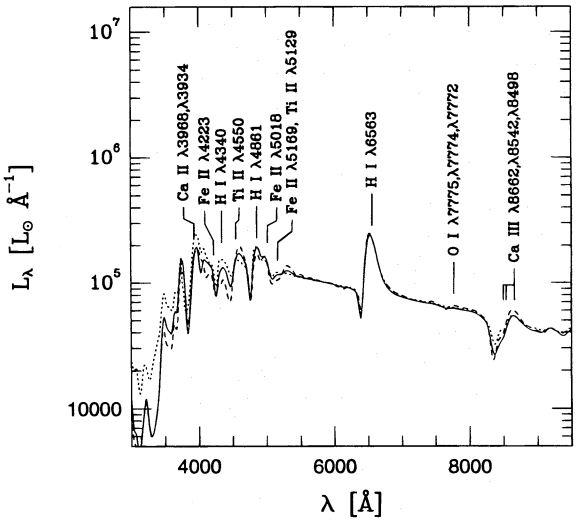

FIG. 13.—This figure shows the effect of metallicity on the emergent spectrum of a recombination phase atmosphere. The abundance of elements heavier than helium are given by their solar mass fraction times a constant *Z*. Shown are spectra of models p6.60.1 (*solid curve*: $n = 6$, $T_{\rm eff} = 4658$ K, $Z = 1$) with models p6.60.3 (*dotted curve*: $Z = 0.3$) and model p6.60.4 (*dashed curve*: $Z = 3$). Large metallicity variations affect mainly the ultraviolet flux and have little effect on the optical continuum at which the opacity is due to electron scattering and photoionization out of the $n = 3$ and $n = 4$ levels of hydrogen.

At early times and higher effective temperature, more energy is emitted in the UV, and we expect a greater sensitivity to *Z*. In Figure 14 are plotted spectra of models s15.19.3 ($T_{\rm eff} = 6630$ K, $Z = 1$) and s15.19.4 ($Z = 0.1$, $T_{\rm eff} = 6763$ K). In this case, there is also a noticeable effect in the UV region, but very little in the optical. Here the UV is not so heavily line blanketed; instead, it is dominated by a smaller number of strong lines of Fe II and Fe III. Decreasing the metallicity by a factor of 10 increased $T_{\rm eff}$ from 6630 K in s15.19.3 to 6763 K in s16.19.4, and the change in optical continuum is within the noise level of most observations.

An extreme case which is unlikely to be observed at low redshift is that of a zero-metallicity Pop III supernova. Figure 15 shows two spectra of model e12.1, one with solar metallicity and the other with zero metallicity. Reducing the metallicity to zero results in an ~12% decrease in the optical continuum, with the energy coming out instead of in

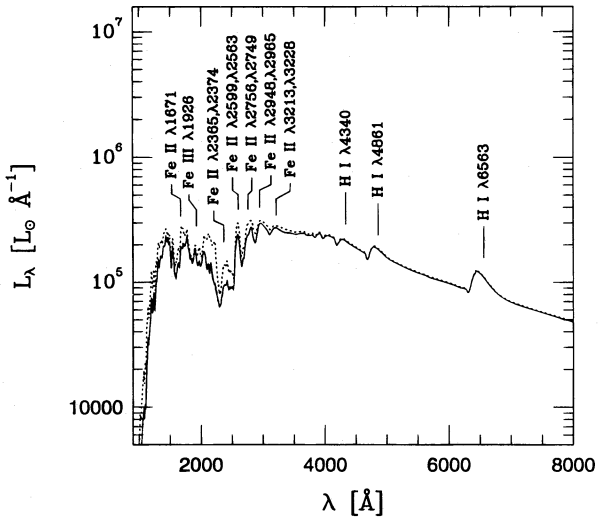

FIG. 14.—The spectra of models s15.19.3 (*solid curve*: $T_{\rm eff} = 6630$ K, $Z = 1$) to model s15.19.4 (*dotted curve*: $Z = 0.1$).

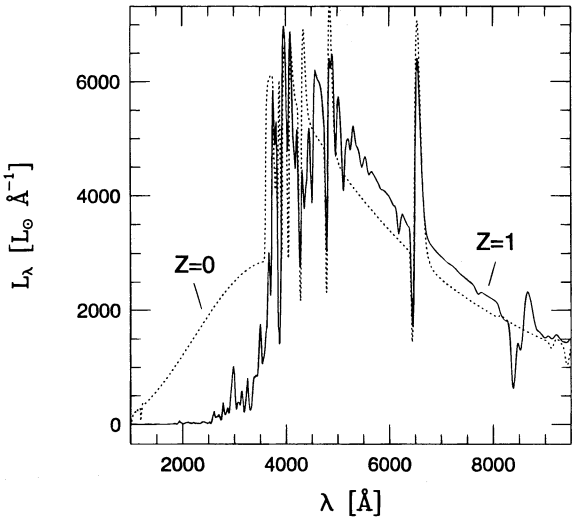

FIG. 15.—Comparison of the emergent spectrum of two exponential atmospheres which differ only in metallicity. One case (*solid curve*) has solar metallicity, while the other (*dotted curve*) has zero metallicity.

the UV. In the zero-metallicity spectrum, the Balmer jump at 3647 Å is clearly discernible, but in the solar metallicty case it is heavily blended with other lines, foiling attempts to use the Balmer jump as a temperature or density diagnostic (Hershkowitz et al. 1986b).

While the abundances of individual heavy elements will affect their individual line strengths, the overall consequences of moderate-metallicity variations for the optical and IR continua are small, and their effects on EPM distances are not of major significance.

3.5. *Luminosity Variation*

The single most important factor influencing overall spectral appearance is the effective temperature. In the context of these simple atmosphere models, the most direct way to bring about a change in $T_{\rm eff}$ is by increasing or decreasing the bolometric luminosity, since by definition $T_{\rm eff} = (L_{\rm bol}/4\pi\sigma_B R_{\rm ph}^2)^{1/4}$. If the atmosphere is in the early hot phase and $T_{\rm eff}$ is high enough to completely ionize H, then $R_{\rm ph}$, which is approximately independent of L, is fixed by the density structure and $T_{\rm eff} \propto L_{\rm bol}^{1/4}$. Therefore, an increase in $L_{\rm bol}$ will have a direct effect on the color temperature and spectral appearance. The lowest temperatures occur when the atmosphere is in the recombination wave phase, $T_{\rm eff} \approx 5 \times 10^3$ K $\approx$ constant, and then $R_{\rm ph} \propto L_{\rm bol}^{1/2}$. An increase or decrease in $L_{\rm bol}$ will scale the spectrum up or down in flux, but it has a modest effect on the appearance of the optical and IR. In the recombination phase, an increase in $L_{\rm bol}$ increases $T_{\rm eff}$ only slightly, and more energy comes out in the UV, but this is mostly due to changes in density as the photosphere is moved inward or outward in a region in which there is a density gradient.

These two effects are illustrated in Figures 16 and 17. In Figure 16 are plotted the spectrum of model s15.12.3, which has $L_{\rm bol} = 3.9 \times 10^{42}$ ergs s^{-1} and $T_{\rm eff} = 7973$ K, model s15.12.1, with $L_{\rm bol} = 6 \times 10^{42}$ ergs s^{-1} and $T_{\rm eff} = 8795$ K,

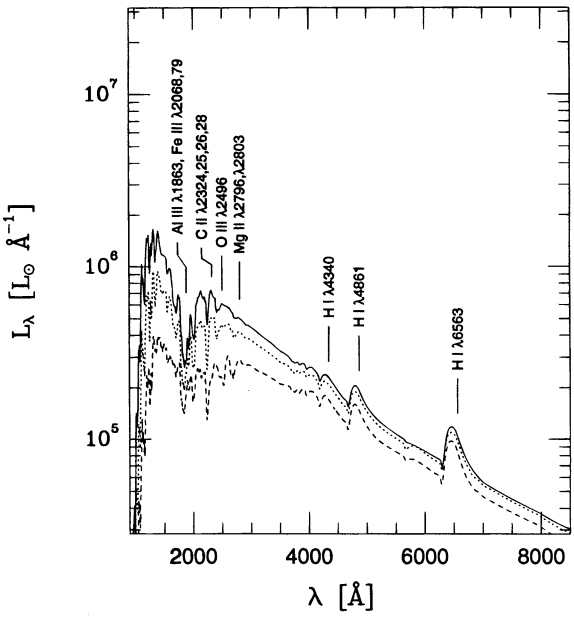

FIG. 16.—The effect of luminosity variation on the emergent spectrum of a selection of s15s2a atmospheres at 12 days after explosion. Shown are the spectra of model s15.12.3 (*dashed curve:* $L = 3.9 \times 10^{42}$ ergs s^{-1}, $T_{\rm eff} = 7973$ K), model s15.12.1 (*dotted curve:* $L = 6 \times 10^{42}$ ergs s^{-1}, $T_{\rm eff} = 8795$ K), and model s15.12.4 (*solid curve:* $L = 8 \times 10^{42}$ ergs s^{-1}, $T_{\rm eff} = 9479$ K).

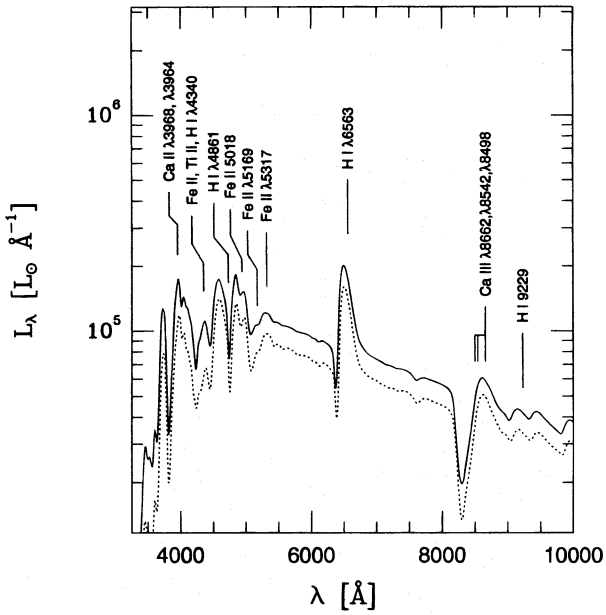

FIG. 17.—The effect of luminosity variation on the spectrum of two s15s2a atmospheres at 43 days after explosion. Shown is the spectrum of model s15.43.1 (*dotted curve:* $L = 1.9 \times 10^{42}$ ergs s^{-1}, $T_{\rm eff} = 4647$ K), and of model s15.43.2 (*solid curve:* $L = 2.5 \times 10^{42}$ ergs s^{-1}, $T_{\rm eff} = 4703$ K).

and model s15.12.4 with $L = 8 \times 10^{42}$ ergs s^{-1} and $T_{\rm eff} = 9479$ K. For this example, a factor of 2 increase in $L_{\rm bol}$ results in nearly the same factor increase in the far-UV. However the optical continuum is in the Rayleigh-Jeans regime, and the flux, $f_\lambda \propto T_{\rm eff} \propto L_{\rm bol}^{1/4}$, increases by 19%.

The effect of an $L_{\rm bol}$ increase on a recombination wave phase model is shown in Figure 17, where we have plotted the spectrum of model s15.43.1, with $L = 1.9 \times 10^{42}$ ergs s^{-1} and $T_{\rm eff} = 4647$ K, and model s15.43.2 with $L = 2.5 \times 10^{42}$ ergs s^{-1}, $T_{\rm eff} = 4703$ K. Although the luminosity in these two models differs by a factor of 1.5, $T_{\rm eff}$ increased by only 1.3% instead of the 7% which would have resulted had $R_{\rm ph}$ remained constant. The main effect of increasing L was to move the photosphere outward in radius by 12%. The change in optical color temperature (§ 4) was comparable to the change in effective temperature.

3.6. *Influence of the Helium Abundance Y*

The abundance of helium is an important quantity in the study of stellar and Galactic chemical evolution. Since there are likely to be large variations in the atmosphere helium abundances of Type II supernovae, it is important to establish the effect this might have on spectral appearance and on distances derived with EPM. The surface helium abundance could be enhanced if the star had lost a substantial amount of mass before explosion, exposing material which was convectively dredged up during core hydrogen burning. The same problems which hamper determination of helium abundance in stars of late spectral type also exist for SNe IIp. From the standpoint of EPM this is a good thing, as it means that distance determinations will not be greatly influenced by uncertain values of Y.

During the plateau phase in which the photosphere is located in the hydrogen envelope, the strongest He absorption is He I λ5876. If the supernova is discovered early enough, the line will still be present, but usually it is weak and disappears when $T_{\rm eff}$ drops below $\sim$8000 K. In the

15 $M_\odot$ model of EWWP, this occurs at ~ 10 days after explosion. Figure 18 shows four spectra from two sets of calculations which give some indication of how the emergent spectrum changes when the Y is varied. The two spectra at the top in Figure 18 are of models p9.10.2 ($Y = 0.25$) and p9.10.3 ($Y = 0.4$). The effective temperature of these models is ~ 8500 K. Changing Y has little effect on the appearance of these spectra, although increasing it from 0.25 to 0.4 causes a slight increase in the effective temperature and a moderate increase in He I λ5876 emission. In both cases, $X_e \sim 1$, so altering Y does not change greatly the position of the electron scattering photosphere. Consequently, the two atmospheres, which have identical luminosities, also have nearly the same effective temperatures. The lower two spectra in Figure 18 are of models p12.10.10 ($Y = 0.40$) and p12.10.11 ($Y = 0.6$). Except for having a steeper density structure ($n = 12$ instead of 9 as in the previous example), the results are similar: except for a modest increase in λ5876 emission, other features in the spectrum remain unaffected.

Below ~ 8000 K, photospheric helium is neutral, mainly in the ground state, and it contributes no opacity at wavelengths $\lambda > 504$ Å. At $T_e < 8000$ K, changes in Y at constant total mass density affect the outcome in the same way as changing the density. Both result in the electron scattering photosphere moving either inward in radius (increased Y or decreased ρ) or outward in radius (decreased Y or increased ρ).

In many of the models listed in Tables 1 and 2, only H was included in the atomic model. The helium equation of state was given by the Saha-Boltzmann equation, and the opacity contribution from He I bound-free was ignored. The validity of this approximation, at least at effective temperatures $T_{\rm eff} \lesssim 8 \times 10^3$ K, is confirmed in Figure 19, which shows spectra of models p6.10.1 (H only) and p6.10.2 (H and He). The two spectra are nearly identical.

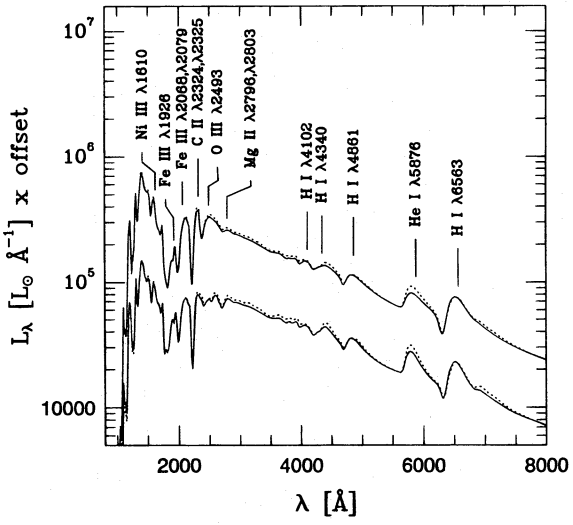

FIG. 18.—The effect of helium abundance on emergent spectrum for effective temperatures $T_{\rm eff} < 10^4$ K. Top: Comparison of model p9.10.2 (*solid curve:* $n = 9$, $T_{\rm eff} = 8458$ K, $Y = 0.25$) with model p9.10.3 (*dotted curve:* $Y = 0.40$). At low $T_{\rm eff}$, the effect of changing Y has little effect and is equivalent to varying the total density and abundances of heavier elements simultaneously. Bottom: Comparison of models p12.10.10 (*solid curve:* $n = 12$, $T_{\rm eff} = 8331$ K, $T = 0.25$) with model p12.10.11 (*dotted curve:* $Y = 0.40$). The weak sensitivity of emergent flux on Y does not change when the power-law density index is changed.

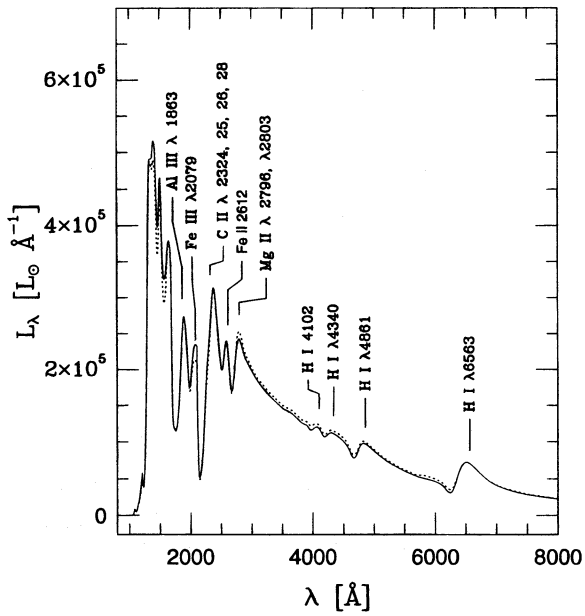

FIG. 19.—These two spectra confirm that the effect of helium bound-free opacity on the emergent spectrum is negligible for temperatures below $\sim 8 \times 10^3$ K. Plotted is the spectrum of models p6.10.1 (*solid curve:* $n = 6$, $T_{\rm eff} = 7721$ K) and p6.10.2 (*dotted curve*), which differs from p6.10.1 only in that departures from LTE in the excitation and ionization of He were included, as was the opacity contribution of He bound-free absorption.

3.7. *Effect of Expansion Rate*

Different explosion energies result in different rates of hydrogen envelope expansion. The total effect on spectral appearance at any one moment will be an alteration of several of the parameters of our model atmospheres. Although it is outside the scope of the present work to pursue this in a physically consistent way, i.e., by blowing up progenitor stars with different explosion energies, we can simulate the effect by simply slowing down the ejecta to provide different kinetic energies.

Figure 20 compares the spectrum of model s15.28.3 with that of model s15.28.4, which is otherwise similar to the former except that the rate of expansion has been slowed by

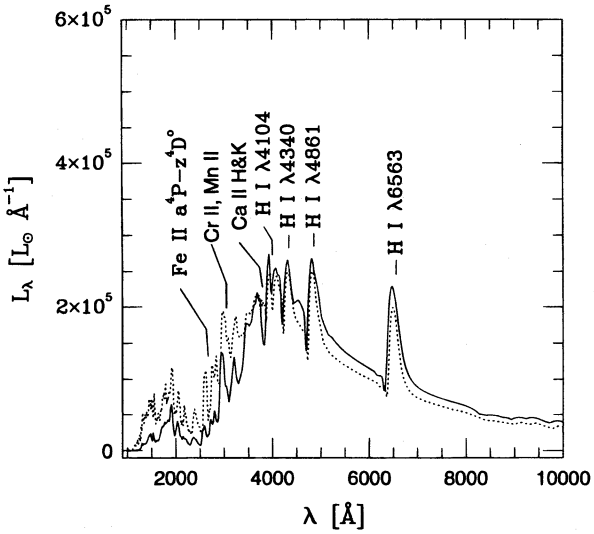

FIG. 20.—Comparison of emergent spectra of models s15.28.3 (*solid curve*) and s15.28.4 (*dotted curve*) in which the expansion velocity has been decreased by a factor of 0.78.

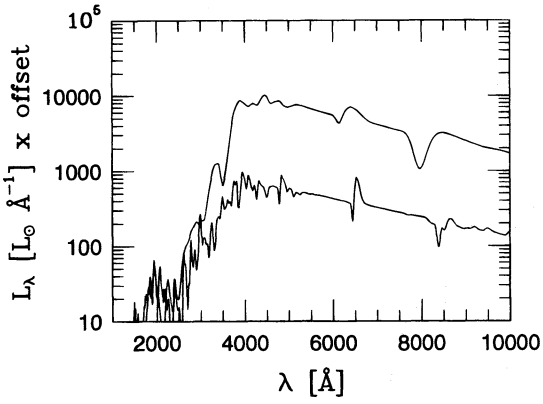

FIG. 21.—This figure compares the spectrum of the two exponential atmosphere models e12.1 and e12.2. The latter model is identical to the former except that the expansion velocity has been increased by a factor of 5. This was functionally identical to resetting the time after explosion from 10^6 s to 2×10^5 s. Besides blueshifting line features and blending them together, it also caused the photosphere to move inward for reasons described in the text.

a factor 0.78, corresponding to a 40% decrease in the explosion energy. Since the luminosity is the same in both calculations, the effect of slowing the expansion rate down is to decrease the radius of the photosphere and increase $T_{\rm eff}$, shifting emission from the optical to the ultraviolet. However, because hydrogen is recombining at the photosphere, the photosphere also moves outward slightly in mass coordinate as a result of the $T_{\rm eff}$ increase, and the radius of the photosphere in model s15.28.4 is only 0.88 times that of model s15.28.3, instead of 0.78 as would be the case if all the gas was ionized.

The other effect of scaling the velocity is, of course, to alter the widths of lines. In Figure 21 are shown the spectra of models e12.1 and e12.2. The latter is identical in every way to the former except that material velocities were increased by a factor of 5. Everything else—the luminosity and mass density vs. radius, etc.—was held fixed. This was formally equivalent to changing the age from 11.6 days to 2.3 days. Besides broadening and blending line absorption and emission features, there is another effect, which is to move the photosphere inward (outward) when v is increased (decreased). The reason for this is that when radiative deexcitation is the predominant exit channel from excited states, the excited state population is inversely proportional to the net downward radiative rate, which is proportional to the expansion velocity. Therefore, increasing the velocity by a factor of 5, as we have done in model e12.2, results in a factor of 5 decrease in the population of the $n = 2$ and $n = 3$ transitions. Since photoionization out of these two levels is the principal ionization mechanism at these effective temperatures, the number of free electrons goes down and the electron scattering photosphere moves inward. The total luminosity was constant in both models; therefore, the effective temperature was higher in model e12.2 than in e12.1 ($T_{\rm eff}$ = 5904 K vs. 5712 K).

4. THE DISTANCE CORRECTION FACTORS AND BOLOMETRIC CORRECTIONS

In this section we use the Type II atmosphere models listed in Tables 1 and 2 to evaluate the distance correction function, ζ_S, which was defined in equation (5). Absolute magnitudes, $M_{\bar{\nu}}$, in $\bar{\nu} = B$, V, Cousins's I_c, and the Johnson infrared bandpasses were determined from model spectra by convolution with analytic filter transmission functions. For B and V, we used the transmission functions of Ažusienis & Straižys (1969), and for I_c we used the transmission function of Bessel (1983). The J, H, and K transmission functions were obtained by multiplying the functions of Johnson (1965) with the transmittance through a model terrestrial atmosphere, as described in Eastman & Kirshner (1989). These are only approximate, but given the smoothness of the IR continuum during the photospheric phase (see Fig. 23 below), they should be adequate.

We have examined four filter combinations: $S = \{BV\}$, $S = \{BVI_c\}$ $S = \{VI_c\}$, and $S = \{JHK\}$. These choices were arrived at through the dual considerations of what is optimal, and what is available. In many cases, especially for historical SN IIp, we have only B and V photometry, so it is important to examine the corrections to EPM distances derived from these bands. None of these choices are fully optimal because line features heavily influence the derived color temperature, especially in B and, to a lesser extent, in V.

The IR is smoother than the optical, and the results of Schmidt et al. (1992) indicated it could be an excellent wavelength range in which to apply EPM. The results presented below suggest that it is excellent for recombination epoch SNe IIp, but also that it should be applied cautiously at early times and to peculiar SNe II. Extensive photometric coverage in the IR is, so far, available for only one SNe II, SN 1987A; however, in the future that is likely to change as data become available for other SNe II as well.

Figure 22 compares the B, V, R_c, and I_c filter transmission functions with two model spectra typifying both an early, high $T_{\rm eff}$ atmosphere and a cooler plateau phase atmosphere. Except at very high $T_{\rm eff}$, the B band is always contaminated to various degrees by H I Balmer line emission. As $T_{\rm eff}$ decreases, a large number of Fe II and Ti II absorptions appear. The V filter rises abruptly near 5000 Å, and so it picks up the Fe II λ5018 and λ5169 absorptions, but it is also sensitive from ~5300 Å to ~6000 Å, which in these spectra are primarily continuum wavelengths. Other Fe II lines and such lines as Na I D also appear at low $T_{\rm eff}$. The Hα line sits firmly inside the R_c band, and because there

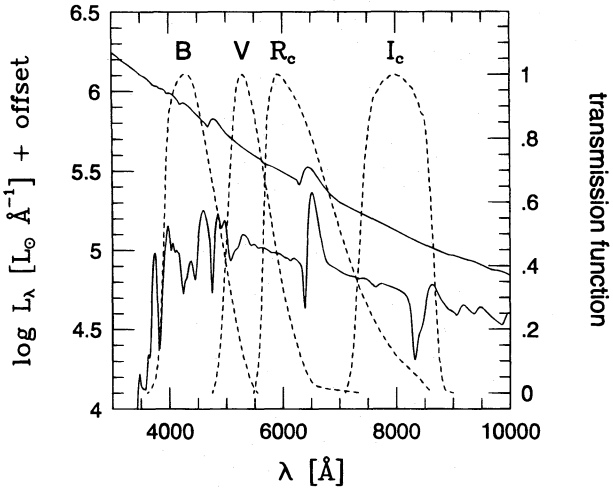

FIG. 22.—Comparison of model spectra (*solid curves*) which typify both the early, high effective temperature phase (model s15.12.5, $T_{\rm eff}$ = 10,190 K, *upper*) and cooler plateau phase (model s15.60.2, $T_{\rm eff}$ = 4550 K, *lower*), with the B, V, R_c and I_c broadband filter transmission functions. The low $T_{\rm eff}$ model has been offset down by 0.5 dex.

is so much variation in SNe II Hα fluxes, it is not a good filter to use for EPM. The Cousins I_c band is less red sensitive than the Johnson I band and includes the region from ~7500 Å to ~8200 Å which is primarily continuum, but unfortunately this also includes the strong Ca II IR triplet lines at 8498, 8548 and 8662 Å.

The 1–2.5 μm region, which encompasses the J, H, and K bands, is primarily a smooth continuum spectrum. Figure 23 compares the three IR transmission functions with spectra of the same two models shown in Figure 22. The only features seen in these spectra are weak H I Paschen lines. There is some contribution to the J-band flux from H I 3–5 and 3–6 emission, but in model s15.60.2 it is less than 5% of the J-band flux.

For the four filter combinations, $S = \{BV\}$, $S = \{VI_c\}$, $S = \{BVI_c\}$, and $S = \{JHK\}$, the color temperature, T_S, and distance correction factor, ζ_S, were computed by minimizing the quantity

$$\mathscr{E} = \sum_{\bar{\nu} \in S} [M_{\bar{\nu}} + 5 \log (R_{\rm ph}/10 \text{ pc}) + 5 \log \zeta_S - b_{\bar{\nu}}(T_S)]^2 , \tag{32}$$

where $b_{\bar{\nu}}(T_S)$ is as defined in equation (8). Its variation with temperature is well fit by a polynomial of the form

$$b_{\bar{\nu}}(T) \approx \sum_{i=0}^{i_{\max}} c_i(\bar{\nu}) \left(\frac{10^4 \text{ K}}{T} \right)^i . \tag{33}$$

For convenience we give, in Table 3, the coefficients of a second-order fit to $b_{\bar{\nu}}(T)$ for $\bar{\nu} = B, V, I_c, J, H, K$, which are accurate to ~0.1% over the range 4000 K ≤ T ≤ 25,000 K.

Figures 24 and 25 compare synthetic spectra and blackbody spectra at the temperatures obtained by minimizing $\mathscr{E}$ (eq. [32]), for the various bandpass combinations. In Figure 24 is shown the spectrum of model s15.5.1, which is a high-ionization model at $T_{\rm eff}$ = 10,190 K, and the best-fitting blackbody spectra. Each of the blackbody spectra agrees well with the model spectrum over the wavelength range they were crafted to fit, but one of the things this figure shows is that as the wavelength range of the fit is shifted further away from the wavelength of peak emission, the apparent color temperature decreases and the best-fit Planck function becomes a progressively poorer description of the whole spectrum. This is because the continuum spectrum falls off more slowly with increasing wavelength than a single-temperature blackbody. There are two separate but related mechanisms which are responsible for this: one is that the continuum opacity increases with increasing wavelength, and consequently the thermalization depth decreases with increasing wavelength and longer wavelength radiation is emitted from shallower optical depths at which the gas temperature is lower. Another mechanism has to do with the Doppler shifts continuum photons undergo between emission and escape. A photon emitted at depth undergoes multiple scatterings before escape and is downshifted in wavelength an amount $\Delta\lambda/\lambda \sim (k_\lambda ct)^{-1}$. Again, since k_λ increases with λ, red photons incur less Doppler shift between emission and escape than blue photons, and this flattens out the emergent spectrum. This process is sensitive to several factors, including both the density and time since explosion.

In ionized, high-T models in which the blue is not heavily line blanketed, $T_{JHK} < T_{VI} < T_{BVI} < T_{BV}$, and T_{JHK} may be either greater than or less than $T_{\rm eff}$, but generalization is

TABLE 3

FITS TO $b_{\bar{\nu}}(T)$[a]

i	$c_i(B)$	$c_i(V)$	$c_i(I_c)$	$c_i(J)$	$c_i(H)$	$c_i(K)$
0.....	−44.36	−43.98	−43.54	−43.15	−43.00	−42.80
1.....	4.19	3.69	3.04	2.66	2.48	2.35
2.....	−0.19	−0.22	−0.28	−0.33	−0.35	−0.37

[a] $b_{\bar{\nu}}(T) = \sum_i c_i(\bar{\nu}) T_4^{-i}$, $T_4 \equiv T/10^4$ K.

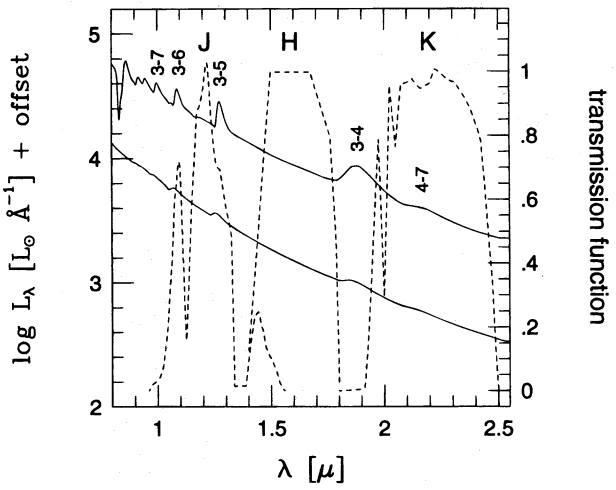

FIG. 23.—Comparison of the 1–2.5 μm spectra of model s15.12.5, ($T_{\rm eff}$ = 10,190 K, *solid curve, lower*) and the cooler plateau phase model s15.60.2 ($T_{\rm eff}$ = 4550 K, *solid curve, upper*), and our J, H, and K broadband filter transmission functions (*dashed curve*). The spectrum of model s15.12.5 has been offset down by 0.5 dex. H I Paschen and Brackett transitions are indicated by lower and upper principal quantum numbers.

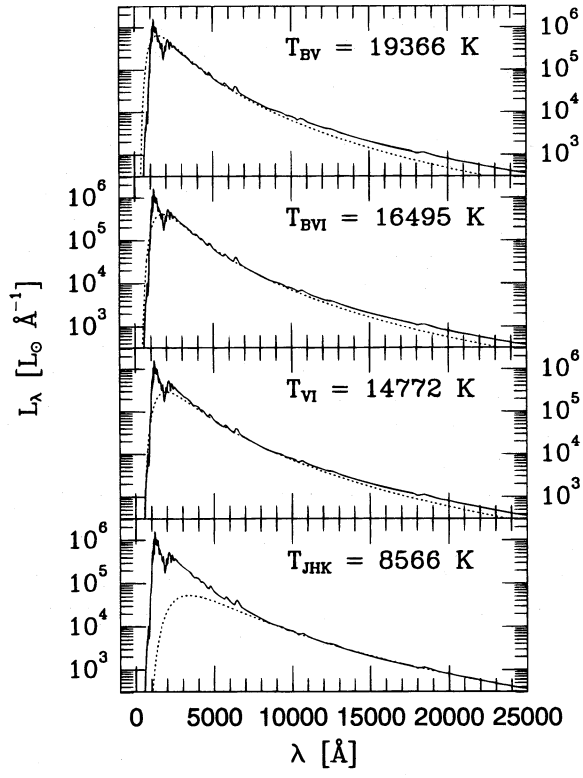

FIG. 24.—Comparison of the spectrum of model s15.5.1 (*solid curve*), which has $T_{\rm eff}$ = 10,190 K, to blackbody spectra (*dotted curve*) obtained by fitting to various bandpass combinations.

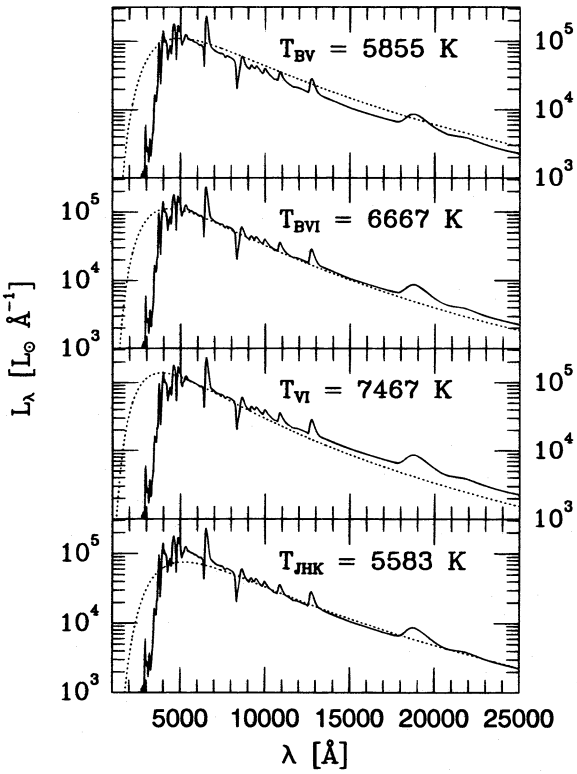

FIG. 25.—Comparison of the spectrum of model s15.60.2 (*solid curve*), which has $T_{\rm eff} = 4550$ K, to blackbody spectra (*dotted curve*) obtained by fitting to various bandpass combinations.

complicated by the different physical mechanisms effecting the color temperature in different wavelength regimes.

Figure 25 compares the spectrum of model s15.60.2, which is a recombination wave model at $T_{\rm eff} = 4550$ K, to the "best-fitting" blackbody spectra. In this case, which characterizes much of the plateau era, color temperatures obtained with B are highly sensitive to the strength of line features. Of the three optical bandpass combinations, BV seems to do the worst job at characterizing the spectrum longward of 6000 Å, although it is still not bad. The renormalized Planck spectrum fit to B and V predicts the flux at 2.5 μm, where the flux is down by a factor of ~ 50, to within 33%. Including the I_c band anchors the fit to the near IR and helps to improve the agreement with the far IR. However, excluding the B band gives a still higher temperature which does not do as well in the IR, and using the IR bands alone gives a much lower temperature, with the result that the optical flux is underestimated by nearly a factor of 2. In both Figures 24 and 25, the IR spectrum is very nearly at the Rayleigh-jeans limit, where $f_\lambda \propto T\lambda^{-4}$, and the derived color temperature is very sensitive to mechanisms such as those discussed above which influence the continuum slope.

No photometry is perfect, and errors in observation can affect the derived color temperature. We can explore this for the two-color case by way of the following: suppose the color derived from photometry in bands $\bar{\nu}$ and $\bar{\nu}'$,

$$C_{\bar{\nu},\bar{\nu}'} \equiv m_{\bar{\nu}} - m'_{\bar{\nu}}\,, \tag{34}$$

has a formal uncertainty $\delta C_{\bar{\nu},\bar{\nu}'}$. Setting

$$C_{\bar{\nu},\bar{\nu}'} \approx b_{\bar{\nu}}(T_{\nu,nu'}) - b_{\bar{\nu}'}(T_{\nu,nu'}) = \sum_{i=0}^{i_{\max}} [c_i(\bar{\nu}) - c_i(\bar{\nu}')]\left(\frac{10^4\ \mathrm{K}}{T}\right) \tag{35}$$

(eq. [33]) and differentiating with respect to $C_{\bar{\nu},\bar{\nu}'}$ gives

$$\frac{\delta T_{\bar{\nu},\bar{\nu}'}}{T_{\bar{\nu},\bar{\nu}'}} = \Delta(T_{\bar{\nu},\bar{\nu}'}) \times \delta C_{\bar{\nu},\bar{\nu}'}\,, \tag{36}$$

where

$$\Delta(T_{\bar{\nu},\bar{\nu}'}) = \left|\sum_{i=1}^{i_{\max}} i[c_i(\bar{\nu}) - c_i(\bar{\nu}')]\left(\frac{10^4\ \mathrm{K}}{T}\right)^i\right|^{-1}. \tag{37}$$

The function $\Delta(T_{\bar{\nu},\bar{\nu}'})$ is plotted in Figure 26 for the three two-color combinations $S = \{BV\}$, $\{VI\}$, and $\{JK\}$, which shows that the higher the temperature, the more sensitive the color temperature is to photometric error, and that the IR, being further out on the Rayleigh-Jeans tail, is more sensitive than the optical. To consider a specific example, at $T_{JK} = 10^4$ K, $\Delta(T_{JK}) = 2.5$. Therefore, to determine T_{JK} to better than 10% the photometry would have to have an accuracy of 4% or better. For $S = \{BV\}$ and $T_{BV} = 10^4$ K, the number is 6%. Although challenging, such precision is now routine with a good CCD or NICMOS camera and moderate size telescope.

Table 4 lists, for each atmosphere model, the effective temperature, the derived color temperature, and the distance correction factor corresponding to each of the four bandpass combinations. The distance correction factors are plotted in Figures 27–30.

For $S = \{BV\}$ (Fig. 27), there is a clear correlation between ζ_{BV} and T_{BV} at low temperature, with ζ_{BV} increasing with decreasing T_{BV}. A nearly identical result was found by Schmidt et al. (1992) for SN 1987A and other SNe II. One might at first be tempted to conclude that as $T_{\rm eff}$ decreases, ζ_{BV} approaches unity. However, examination of the top panel of Figure 2 shows that roughly half the models are near the hydrogen recombination temperature and have $T_{\rm eff} \sim 5000$ K. Although there is little variation in $T_{\rm eff}$ in those models, there is a large variation in density at the photosphere. Figure 31 compares the ratio $T_S/T_{\rm eff}$ to $\rho_{\rm ph}$ for each filter combination. In the context of a simple continuum scattering model, when the thermalization depth lies deep inside the photosphere this ratio will be large, and vice versa. Although we do not expect it to be a simple

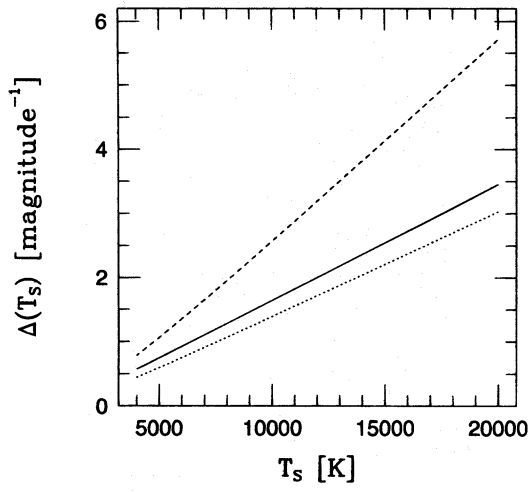

FIG. 26.—This figure shows $\Delta(T_S)$, which is the relative uncertainty in color temperature per unit uncertainty in photometric color (eq. [37]) for the bandpass combinations $S = \{BV\}$ (*solid line*), $S = \{VI\}$ (*dotted line*), and $S = \{JK\}$ (*dashed line*).

TABLE 4

COLOR TEMPERATURES AND DISTANCE CORRECTION FACTORS

Model	$T_{\rm eff}$	T_{BV}	ζ_{BV}	T_{BVI}	ζ_{BVI}	T_{VI}	ζ_{VI}	T_{JHK}	ζ_{JHK}
p6.10.1	7721	10498	0.50	11246	0.45	11925	0.43	6223	0.85
p6.10.2	7820	11226	0.46	11571	0.44	11860	0.43	6435	0.81
p6.40.1	4480	4287	1.57	5592	0.69	7193	0.45	5543	0.69
p6.40.2	4838	6929	0.55	7618	0.45	8258	0.40	5766	0.67
p6.40.3	4625	5266	0.94	6406	0.56	7660	0.43	5692	0.67
p6.60.1	4658	7799	0.41	7752	0.41	7719	0.42	5901	0.60
p6.60.2	4705	7055	0.50	7253	0.47	7419	0.46	5918	0.63
p6.60.3	4732	8046	0.39	7660	0.43	7398	0.46	5905	0.62
p6.60.4	4706	6542	0.59	7046	0.50	7498	0.46	5929	0.63
p6.60.5	4528	5766	0.72	6460	0.54	7096	0.47	5928	0.62
p6.60.6	4716	7133	0.49	7302	0.47	7439	0.46	5901	0.60
p9.10.1	8411	13069	0.42	12907	0.43	12773	0.43	6921	0.82
p9.10.2	8458	12885	0.44	12782	0.44	12703	0.45	7013	0.83
p9.10.3	8546	12784	0.45	12867	0.45	12936	0.45	7109	0.82
p9.10.4	9231	14163	0.42	14143	0.42	14135	0.42	7035	0.84
p9.60.1	4791	7050	0.52	7074	0.51	7096	0.51	5946	0.66
p12.10.1	8195	13882	0.39	12670	0.44	11851	0.47	7035	0.83
p12.10.2	8254	13767	0.41	12662	0.45	11893	0.48	7118	0.82
p12.10.3	9422	16475	0.37	14194	0.44	12806	0.49	7118	0.89
p12.10.4	6742	11860	0.38	10945	0.43	10314	0.46	6579	0.77
p12.10.5	9398	15934	0.38	14481	0.43	13497	0.46	7266	0.86
p12.10.6	10552	17896	0.37	16055	0.42	14845	0.45	7428	0.88
p12.10.7	11135	19053	0.36	16923	0.41	15551	0.44	7513	0.89
p12.10.8	9425	14999	0.42	14158	0.45	13547	0.47	7398	0.86
p12.10.9	10585	16998	0.40	15694	0.44	14785	0.46	7540	0.89
p12.10.10.....	8331	13360	0.43	12670	0.46	12172	0.48	7210	0.83
p12.10.11.....	8434	13323	0.44	12770	0.47	12357	0.48	7270	0.83
p12.60.1	4819	6523	0.61	6689	0.57	6827	0.55	5637	0.72
s15.5.1.....	12711	18427	0.47	16055	0.55	14573	0.60	6378	1.25
s15.12.1	8795	15243	0.38	13588	0.43	12518	0.47	7443	0.80
s15.12.2	8940	15348	0.40	13688	0.46	12601	0.50	7306	0.85
s15.12.3	7973	14209	0.37	12593	0.44	11549	0.48	7197	0.79
s15.12.4	9479	16828	0.35	14484	0.42	13060	0.47	7324	0.83
s15.12.5	9610	16517	0.39	14586	0.45	13351	0.49	7439	0.87
s15.19.1	6186	11923	0.34	10452	0.41	9547	0.46	6529	0.72
s15.19.2	6772	13308	0.32	11329	0.40	10162	0.46	6579	0.75
s15.19.3	6378	11511	0.39	10586	0.45	9959	0.48	6378	0.80
s15.19.4	6763	11623	0.40	10646	0.45	9990	0.49	6398	0.80
s15.19.5	7139	13882	0.32	11654	0.40	10361	0.46	6603	0.76
s15.19.6	7647	14619	0.32	12310	0.40	10959	0.45	6750	0.77
s15.20.1	6284	11678	0.36	10437	0.43	9636	0.47	6689	0.71
s15.28.1	5303	8711	0.47	9026	0.44	9293	0.43	5842	0.75
s15.28.2	5514	9549	0.42	9506	0.43	9466	0.43	5914	0.75
s15.28.3	5416	10210	0.35	9439	0.39	8910	0.42	6140	0.68
s15.28.4	5767	11540	0.31	10004	0.39	9070	0.44	6153	0.70
s15.28.5	5336	10238	0.33	9186	0.40	8521	0.44	5974	0.69
s15.40.1	4908	7281	0.52	7531	0.48	7735	0.46	6107	0.66
s15.43.1	4647	5974	0.70	6772	0.52	7540	0.44	5692	0.67
s15.43.2	4703	6714	0.56	7270	0.47	7769	0.42	5695	0.66
s15.43.3	4811	5730	0.91	6921	0.57	8237	0.44	5625	0.75
s15.46.1	4785	6643	0.59	7201	0.50	7711	0.45	5929	0.65
s15.46.2	4778	6085	0.74	7247	0.49	8512	0.39	5583	0.69
s15.60.1	4093	4132	1.45	5418	0.61	7004	0.39	5177	0.62
s15.60.2	4422	5855	0.66	6667	0.48	7467	0.40	5583	0.62
s15.60.3	4512	5054	1.11	6037	0.68	7055	0.52	5628	0.72
s15.60.4	4743	7017	0.52	7279	0.48	7480	0.46	5901	0.66
s25.5.1.....	17875	17735	0.74	16897	0.78	16267	0.81	10133	1.22
s25.30.1	6008	11387	0.34	9506	0.45	8438	0.53	6116	0.77
s25.60.1	4754	7544	0.44	7281	0.47	7096	0.49	5890	0.62
10h.30.1	4972	5800	0.87	6495	0.66	7138	0.57	5905	0.74
10h.60.1	4651	5813	0.73	6258	0.60	6638	0.55	5822	0.66
e12.1.....	5558	7821	0.61	7843	0.60	7868	0.60	6320	0.80
e12.2.....	5904	7387	0.86	8832	0.60	10507	0.49	7439	0.81
e12.3.....	5551	8943	0.47	8633	0.50	8414	0.52	6350	0.77

function of one variable only, there is a clear correlation of $T_{BV}/T_{\rm eff}$ to $\rho_{\rm ph}$. This is mostly due to the increased amount of line blanketing in the B band at higher density. A secondary effect ought to be that as density increases, the importance of absorptive opacity over scattering increases, and the emergent flux becomes less dilute and closer to the Planck function at $T_{\rm eff}$. If this mechanism were important, then $T_{JHK}/T_{\rm eff}$ would also correlate with $\rho_{\rm ph}$, but there is a trend of weaker correlation with $\rho_{\rm ph}$ at longer wavelength. The reason for this is that the ratio of continuum absorptive opacity to scattering opacity, which fixes the thermalization depth and amount of flux dilution, is far more sensitive to

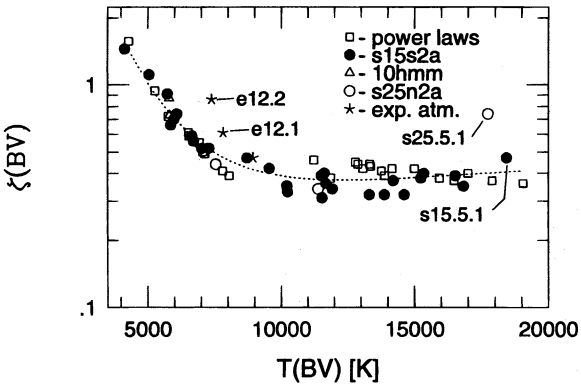

FIG. 27.—Distance correction factors derived from $S = \{BV\}$ photometry (ζ_{BV}) for the models in Tables 1 and 2 are plotted vs. derived color temperature (T_{BV}). Dashed curve is a second-order polynomial in T_{BV}^{-1}.

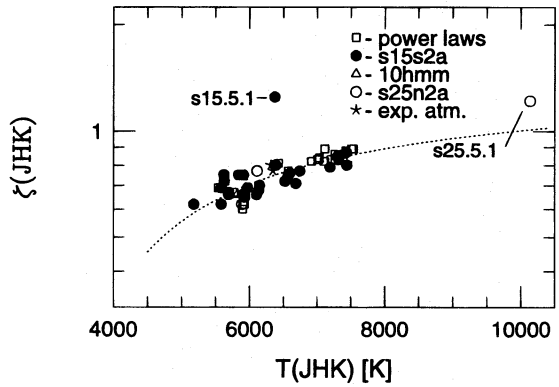

FIG. 30.—Same as Fig. 27, but for $S = \{JHK\}$, and the polynomial fit is first order in T_{JHK}^{-1}.

the effective temperature than to density, and this masks almost completely the dependence on ρ_{ph}. Figure 32 compares T_S/T_{eff} to T_{eff} for each filter combination. Again, in B the dominant factor is ρ_{ph}, so there appears to be little or no correlation between T_{BV}/T_{eff} and T_{eff}. However, in the IR where line blanketing is much less important, a very strong correlation can be seen. At high ionization, the electron density, which accounts for the scattering part of the opacity, is just proportional to the total density. The absorptive continuum opacity, however, is due mainly to photoionization out of the $n = 3$ and $n = 4$ levels of H I. Assuming $T^4 \propto T_{eff}^4 \tau$ and using equation (6) for τ_{thrm}, it follows that $T_S/T_{eff} \propto (N_e/N_n)^{1/8}$, where N_n is the population of hydrogen level n. Figure 33 illustrates how $(N_e/N_3)^{1/8}$ and $(N_e/N_4)^{1/8}$ vary with temperature in LTE when the total density is fixed. In the example of Figure 33, $(N_e/N_3)^{1/8}$ and $(N_e/N_4)^{1/8}$ decrease with T until a minimum is reached near 7000 K and increase afterward. In Figure 32, T_{JHK}/T_{eff} is still decreasing at $T_{eff} > 10^4$ K, which is explained by the fact that the excitation is not in strict LTE.

The dashed lines in Figures 27–30 are least-square polynomial fits to ζ_S given by $\zeta_S(T_S) \approx z(T_S)$, were T_S is the rele-

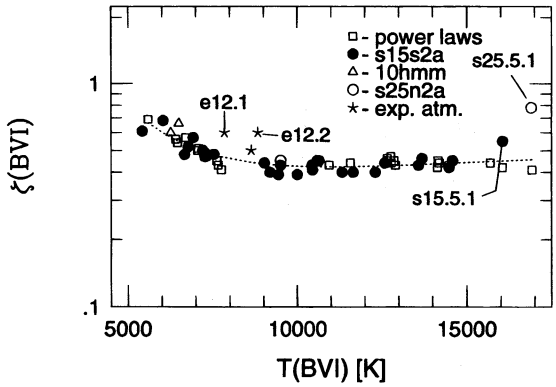

FIG. 28.—Same as Fig. 27, but for $S = \{BVI\}$

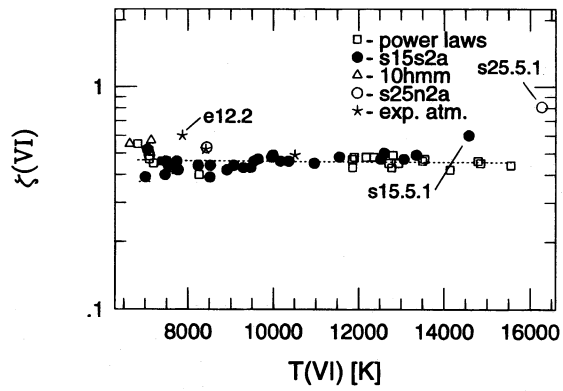

FIG. 29.—Same as Fig. 27, but for $S = \{VI_c\}$, and the polynomial fit is first order in T_{VI}^{-1}.

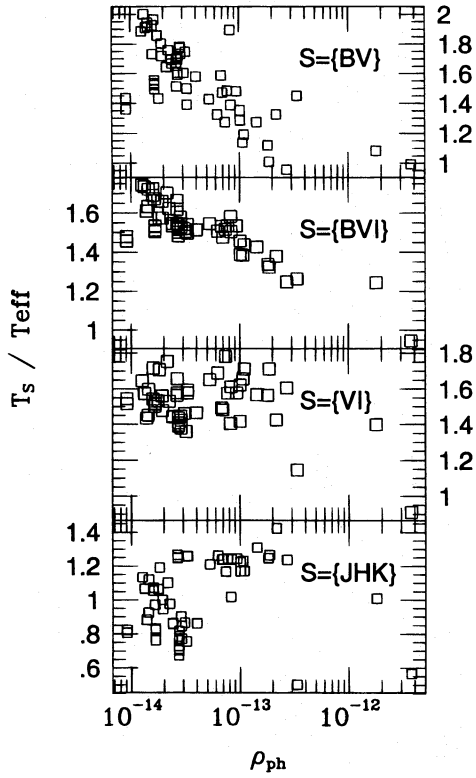

FIG. 31.—This figure examines how well T_S/T_{eff} correlates with density at the photosphere. Line blanketing, which affects B and V, is sensitive to the gas density. Higher density atmospheres are more highly line blanketed, and therefore they give a lower color temperature which is closer to the actual effective temperature. The infrared, which is essentially pure continuum, is far more sensitive to temperature, which masks the much weaker density dependence.

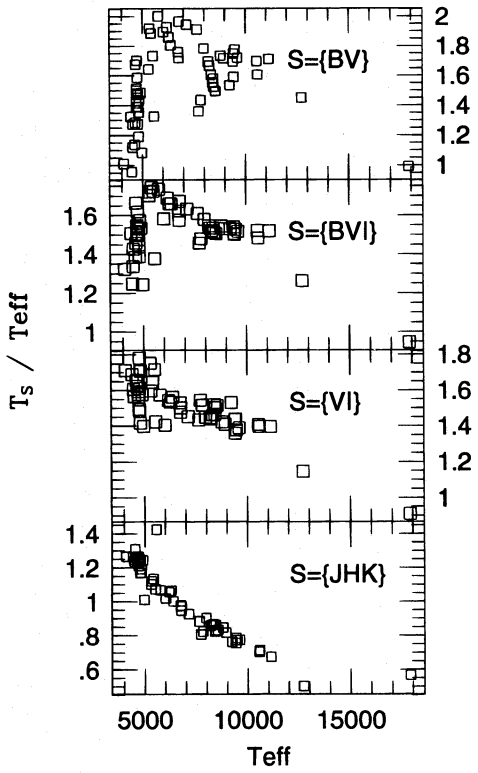

FIG. 32.—This figure examines how well $T_S/T_{\rm eff}$ correlates with $T_{\rm eff}$. Whereas there is weak or no correlation between $T_{BV}/T_{\rm eff}$ and $T_{\rm eff}$, there is clearly a strong correlation in the infrared.

vant color temperature for each bandpass combination and

$$z(T_S) = \sum_{j=0}^{j_{\max}} a_{S,j} \left(\frac{10^4 \text{ K}}{T_S} \right)^j . \tag{38}$$

An important result of this work is that the mean difference between ζ and the smooth polynomial temperature fits are very small: for $S = \{BV\}$, $\sigma \equiv \langle (\zeta - z)^2/\zeta^2 \rangle^{1/2} = 0.11$; for $S = \{BVI\}$, $\sigma = 0.05$; for $S = \{VI\}$, $\sigma = 0.08$; and for $S = \{JHK\}$, $\sigma = 0.07$. Excluding the four peculiar models e12.1, e12.2, s15.5.1, and s25.5.1 (see below), the maximum discrepancy is as follows: for $S = \{BV\}$, max $(\zeta - z) = 0.24$; for $S = \{BVI\}$, max $(\zeta - z) = 0.17$; for $S = \{VI\}$, max $(\zeta - z) = 0.19$; and for $S = \{JHK\}$, max $(\zeta - z) = 0.15$. If the explosion models employed in this study are at all representative of conditions in actual SNe IIp, then distances based on B, V, and I photometry should be especially good, with θ measurements accurate to $\sim 10\%$ at the 2 σ level.

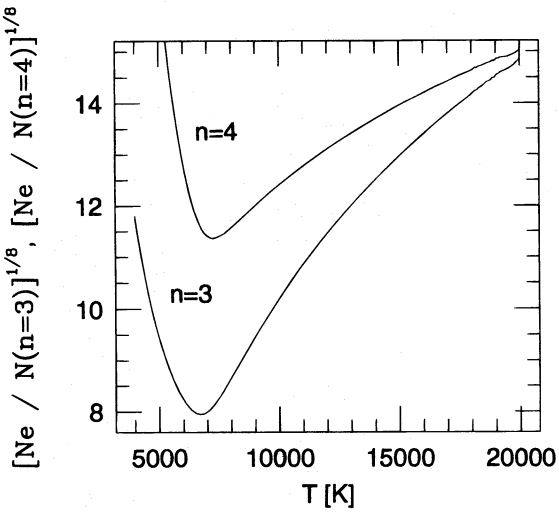

FIG. 33.—This figure shows $(N_e/N_3)^{1/8}$ and $(N_e/N_4)^{1/8}$ as a function of gas temperature, assuming LTE and a total number density of hydrogen atoms of 10^{11} cm^{-3}. For continua only, the minimum temperature of these functions corresponds to the temperature at which the emergent spectrum is the least dilute relative to the best-fitting blackbody.

Although there is a spread in ζ_S values about the polynomial fits in Figures 27–30, four models in particular stand out as being substantially different. Two of these are the exponential atmosphere models e12.1 and e12.2. Model e12.1 corresponds to a 1.84 $M_\odot$ star with 4×10^{49} ergs of kinetic energy, which is not an appropriate model for a Type II plateau supernova, and model e12.2 is exactly the same as e12.1, but with expansion velocity boosted by a factor of 5. Spectra of both models are shown in Figure 21. In addition, as we mentioned in § 3, models s15.5.1 and s25.5.1 are distinguished by being very steep ($d \ln \rho / d \ln r \approx -26$ and -88, respectively). Spectra of these two models are shown in Figure 20. These two models also have high effective temperature, and all four of these models are high density compared to most other models in our sample. Although it is possible that conditions such as are represented by models s15.5.1 and s25.5.1 might be observed in SNe IIp shortly after explosion, they would be easy to identify spectroscopically and the observations would be excluded from use in distance determinations.

Density has two effects on T_S and on ζ_S. As Figure 31 suggests, it affects T_{BV} in recombination epoch models by modulating the amount of line blanketing in B. For homologous expansion, the Sobolev optical depth of lines is proportional to ρt, so it is actually the product of these two quantities which control T_{BV}, and T_{BVI}. An entirely separate effect of density is how it influences the amount of dilution in the underlying continuum. There is no apparent correlation between $T_{JHK}/T_{\rm eff}$ and $\rho_{\rm ph}$ in Figure 31, and since the IR is nearly pure continuum, this suggests that the influence of density on continuum dilution is small. In order to explore this, we have modified equation (38) to take into account density variation at the photosphere:

$$\zeta_S \approx \tilde{\zeta}_S(\rho_{\rm ph}, T_S) \equiv \rho_{\rm ph}^{\gamma} z(T_S) , \tag{39}$$

where $\rho_{\rm ph}$ is tabulated in Tables 1 and 2 for each model, and $z(T_S)$ is as given in equation (38). The effect of $\rho_{\rm ph}$ on T_S from the blanketing is included implicitly in $z(T_S)$, so the additional $\rho_{\rm ph}^{\gamma}$ term ought to reflect the changes in the continuum dilution with changes in density. This is, admittedly, somewhat crude, but it is adequate for our present purpose.

A rough LTE analysis predicts two limiting behaviors for γ in equation (39), corresponding to the two limits of high temperature/high ionization, and low temperature/low ionization: as discussed in § 1, $\zeta \sim \tau_{\rm thm}^{1/2} \propto (k_\nu / N_e \sigma_T)^{1/4}$ (eq. [6]). In the highly ionized extreme, $N_e \propto \rho$ and $k_\nu \propto \rho^2$; therefore, we would expect $\zeta \propto \rho^{1/4}$. In the low-ionization limit, $N_e \propto \rho^{1/2}$ and $k_\nu \propto \rho$, and in that case $\zeta \propto \rho^{1/8}$. This would be the situation if the gas were in LTE and excitation-ionization were given by the Saha-Boltzmann equation. In reality, neither the dilute radiation field nor low electron density are sufficient to drive photospheric gas into thermodynamic equilibrium. It should also be noted that, for the high-ionization case, Montes & Wagoner (1995) obtained the analytic result that $\zeta \propto \Delta R^{-1/6}$, and since $\Delta R \sim 2/(3\rho_{\rm ph})$, this then implies $\zeta \propto \rho_{\rm ph}^{1/6}$.

The results of fitting equation (39) to the ζ_S values in Table 4 are plotted in Figures 34 through 37, and the fitting parameters are listed in Table 5, not only for equation (39), but also for the case in which γ has been set equal to zero (eq. [38]). In the upper panel of each figure we show, for all models, the value of ζ from Table 4, plotted against color temperature, and also the predicted value based on the fit to equation (39). The T_S dependence, $z(T_S) = \tilde{\zeta}/\rho_{\rm ph}^{\gamma}$, is plotted as a dotted line in each figure. The lower panel shows the percent error in the fit, i.e., $100 \times (\zeta_S - \tilde{\zeta}_S)/\zeta_S$. In performing this fit, we have also included models s15.5.1, s25.5.1, and e12.1, which were excluded in the $\gamma = 0$ case. With the exception of the infrared, including the $\rho_{\rm ph}^{\gamma}$ term improves the agreement between ζ_S and $\tilde{\zeta}_S$ for the high-density models such as s15.5.1 and s25.5.1. For all four filter combinations, the derived value of γ is very small, varying from

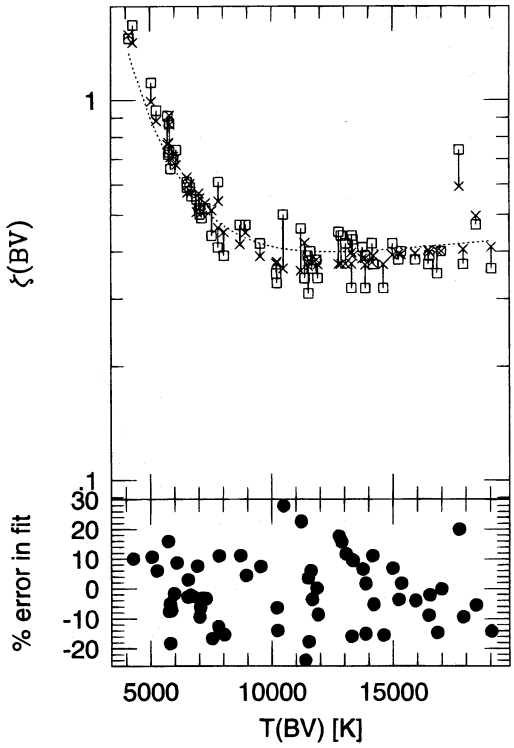

FIG. 34.—*Top:* Distance correction factors for the bandpass combination $S = \{BV\}$, vs. BV color temperature. The squares are the model results from Table 4. Crosses connected to squares by solid lines show the value of ζ_{BV} computed by fitting eq. (4.4) to the values of Table 4. Dashed line shows the derived temperature variation, $z(T_{BV})$, which is a second-order polynomial (vertically scaled). *Bottom:* Difference between computed and fit value of ζ_{BV}, in percent.

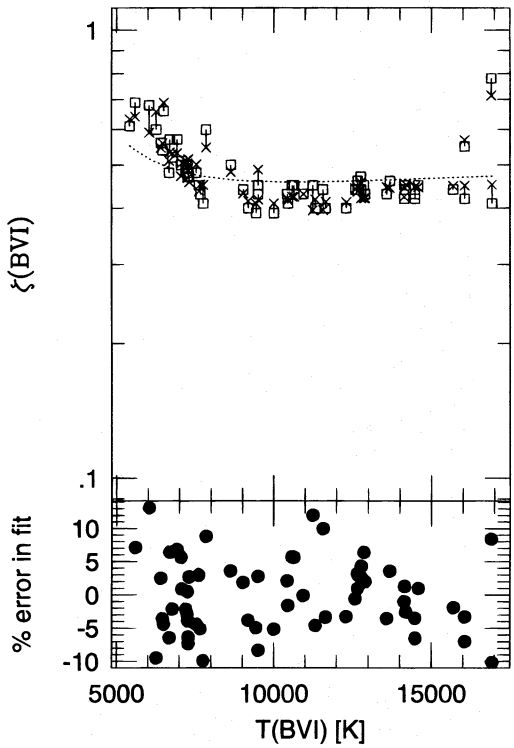

FIG. 35.—Same as Fig. 34, except $S = \{BVI\}$

$\sim 1/11$ for $\{BVI\}$ to $\sim 1/33$ for $\{JHK\}$. The small IR density dependence is consistent with the weak correlation between $T_{JHK}/T_{\rm eff}$ and $\rho_{\rm ph}$ shown in Figure 31. Once again, the best result (smallest residuals) is obtained for $S = \{BVI\}$. This is not surprising because, as we indicated earlier, $\{BVI\}$ does the best job of producing a single blackbody temperature which fits the 4000 Å to 2.5 μm spectral range. It takes advantage of the most information, including where the spectrum peaks.

Recently, Montes & Wagoner (1995) carried out a semi-analytic analysis of how ζ ought to vary in SNe II photospheres represented as power-law density structures. It is difficult to compare directly the magnitude of their predicted ζ with ours because they defined color temperature and ζ differently from us, using instead $\zeta_\nu = [F_\nu/\pi B_\nu(T_{{\rm thm},\nu})]^{1/2}$, where $B_\nu(T)$ is the Planck function, $T_{{\rm thm},\nu}$ is the gas temperature at the thermalization depth (eq. [27]), and F_ν is the emergent flux. Although they did include an approximate representation of line opacity, it was a smoothly varying function, and their definition of ζ is appropriate for investi-

TABLE 5

COEFFICIENTS OF PARAMETRIC ζ FIT[a]

	BV		*BVI*		*VI*		*JHK*	
PARAMETER	$\gamma = 0$	$\gamma = 7.76 \times 10^{-2}$	$\gamma = 0$	$\gamma = 9.33 \times 10^{-2}$	$\gamma = 0$	$\gamma = 7.69 \times 10^{-2}$	$\gamma = 0$	$\gamma = 3.07 \times 10^{-2}$
a_0	6.74×10^{-1}	6.68×10^{-1}	6.86×10^{-1}	6.05×10^{-1}	4.45×10^{-1}	5.92×10^{-1}	1.45	1.64
a_1	-7.41×10^{-1}	-6.05×10^{-1}	-5.77×10^{-1}	-2.34×10^{-1}	1.36×10^{-2}	-8.64×10^{-2}	-4.50×10^{-1}	-5.51×10^{-1}
a_2	4.56×10^{-1}	3.77×10^{-1}	3.16×10^{-1}	1.24×10^{-1}	...	...	...	...
σ[b]	0.11	0.11	0.05	0.06	0.08	0.08	0.07	0.09
max $(\lvert\zeta - \tilde{\zeta}\rvert/\zeta)$...	0.24	0.28	0.17	0.13	0.19	0.26	0.15	0.35

NOTE.—Models e12.1, s15.5.1, and s25.5.1 were only included in the $\gamma \neq 0$ fit.

[a] $\tilde{\zeta}(\rho_{\rm ph}, T_S) = (\rho_{\rm ph}/10^{-13}\ {\rm g\ cm^{-3}})^{\gamma} \sum_i a_i \times (10^4\ {\rm K}/T_S)^i$.

[b] σ = rms relative difference between ζ and $\tilde{\zeta}$.

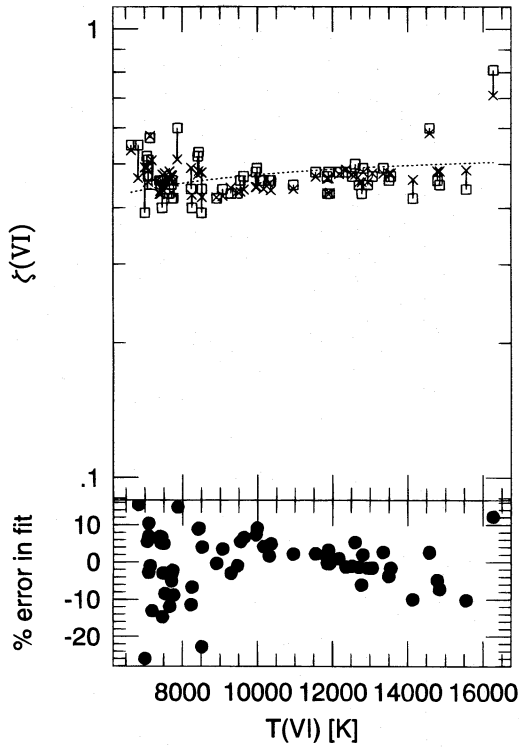

FIG. 36.—Same as Fig. 34, except $S = \{VI\}$, and $z\{T_{VI}\}$ is first order

gating continuum dilution, and not the effect which line blanketing has on the apparent color temperature. Their high $T_{\rm eff}$ results are in good qualitative agreements with ours, predicting that ζ should be roughly independent of $T_{{\rm thm},\nu}$. And at low $T_{{\rm thm},\nu}$ (their low-ionization, recombination wave case), they predict the same type of behavior as we obtain for $S = \{JHK\}$, which is our only pure continuum case. They find also that ζ decreases with decreasing $T_{{\rm thm},\nu}$. In addition, they find that the sensitivity of ζ to both the density and its gradient is very small. This is a very important result because it means that equation (38), with the coefficients given in Table 5 ($\gamma = 0$), may be used to correct for flux dilution and thereby determine the distance to SNe IIp without having to account for variations between individual supernovae.

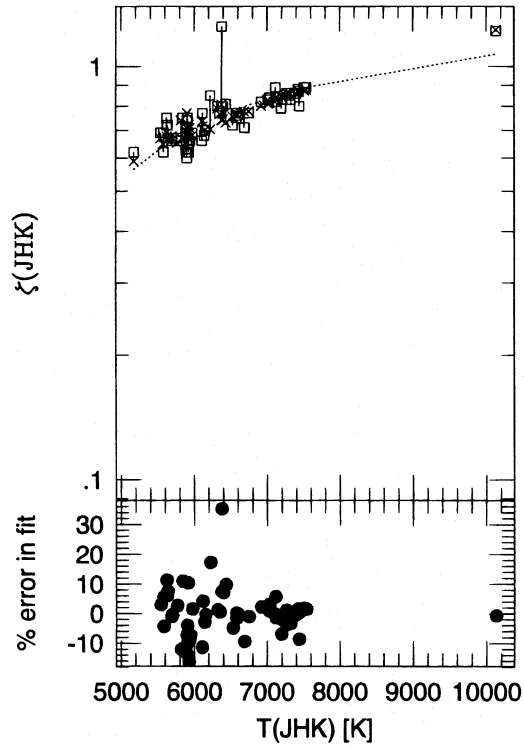

FIG. 37.—Same as Fig. 34, except $S = \{JHK\}$, and $z(T_{JHK})$ is first order

5. THE EFFECT OF DUST EXTINCTION ON THE DERIVED PHOTOMETRIC ANGULAR SIZE

It is all but certain that Type II plateau supernovae originate from red supergiant stars with masses $M \gtrsim 10\ M_\odot$. They are likely, therefore, to be found near or within the dusty molecular cloud complexes from whence they formed, and the light which arrives at Earth to be heavily reddened. Extinction from intervening dust is the bane of standard-candle distance methods. Since the apparent colors observed of SNe IIp could potentially be quite different from the intrinsic ones, it behooves us to inquire as to what extent this will affect the derived distance, or more specifically, the measurement of photospheric angular size.

For EPM, dust turns out to be far less of a problem than it is for standard-candle techniques. This is because dust effects the observed SN spectrum in two ways. First, it decreases the amount of light received, thus making a supernova appear further away. Second, the differential extinction makes the photosphere appear cooler, less luminous, and therefore closer. The two effects tend to cancel out. This was established empirically by Schmidt et al. (1992), who showed that distances derived with EPM change by $\sim 10\%$ or less when the assumed visual extinction is varied by a magnitude. It is straightforward to show analytically why this should be so. Consider the application of EPM with just two bandpasses, such as B and V. To first order in $1/T$, the apparent magnitude in band $\bar{\nu}$ can be written

$$m_{\bar{\nu}} = c_0(\bar{\nu}) + c_1(\bar{\nu})\frac{10^4\ {\rm K}}{T} + R(\bar{\nu})E(B-V) - 5\log(\theta\zeta)\ , \tag{40}$$

where $R(\bar{\nu}) \equiv A(\bar{\nu})/E(B-V)$ is the ratio of extinction in bandpass $\bar{\nu}$ to the $B-V$ color excess. For B, V, and I_c, these coefficients are $c_0(B) \approx -44.09$, $c_1(B) \approx 3.68$, $R(B) \approx 4.1$, $c_0(V) \approx -43.67$, $c_1(V) \approx 3.06$, $R(V) \approx 3.1$, $c_0(I_c) \approx -43.15$, $c_1(I_c) \approx 2.29$, and $R(I_c) \approx 2.3$. The R-values are from Savage & Mathis (1979).

Using equation (40), the color temperature is given by

$$\begin{aligned} C_{\bar{\nu},\bar{\nu}'} &\equiv m_{\bar{\nu}} - m_{\bar{\nu}'} \\ &= [c_0(\bar{\nu}) - c_0(\bar{\nu}')] + [R(\bar{\nu}) - R(\bar{\nu}')]E(B-V) \\ &\quad + [c_1(\bar{\nu}) - c_1(\bar{\nu}')]\frac{10^4\ {\rm K}}{T_{\bar{\nu},\bar{\nu}'}}\ . \end{aligned} \tag{41}$$

Solving for $1/T_{\bar{\nu},\bar{\nu}'}$ and plugging back into equation (40) gives

$$\begin{aligned} 5\log(\theta\zeta) = c_0(\bar{\nu}) - m_{\bar{\nu}} &+ \frac{c_1(\bar{\nu})}{c_1(\bar{\nu}) - c_1(\bar{\nu}')} \\ &\times \{C_{\bar{\nu},\bar{\nu}'} - [c_0(\bar{\nu}) - c_0(\bar{\nu}')] \\ &- [R(\bar{\nu}) - R(\bar{\nu}')]E(B-V)\} \\ &+ R(\bar{\nu})E(B-V)\ . \end{aligned} \tag{42}$$

The sensitivity of $\log(\theta\zeta)$ to uncertain extinction corrections is determined by the derivative

$$\frac{\partial \ln(\theta\zeta)}{\partial E(B-V)} = \frac{c_1(\bar{\nu})R(\bar{\nu}') - c_1(\bar{\nu}')R(\bar{\nu})}{5\ln(10)[c_0(\bar{\nu}) - c_0(\bar{\nu}')]} . \quad (43)$$

Taking $\bar{\nu} = B$ and $\bar{\nu}' = V$ and using the coefficients given above, this becomes

$$\frac{\partial \ln(\theta\zeta)}{\partial A(V)} = \frac{1}{R(V)} \frac{\partial \ln(\theta\zeta)}{\partial E(B-V)} \approx 0.08 , \quad (44)$$

i.e., for a 1 mag uncertainty in visual extinction, the value of $\theta\zeta$ is uncertain by only 8%. The above analysis explains the low sensitivity of derived distance to A_V found by Schmidt, et al. (1992).

Using $\bar{\nu} = V$ and $\bar{\nu}' = I_c$, this becomes

$$\frac{\partial \ln(\theta\zeta)}{\partial A(V)} \approx 3 \times 10^{-3} . \quad (45)$$

This is an astounding result. EPM's robust insensitivity to uncertain reddening corrections is unique among distance indicators.

At very high temperatures, the optical continuum is on the Rayleigh-Jeans tail of the Planck spectrum at which optical colors are independent of temperature, and the color temperature becomes indeterminate. In the limit $T \to \infty$, $\partial \ln f_\lambda / \partial \ln \lambda \sim -4$, independent of T. If this is suspected to be the case, then the intrinsic colors are known and the extinction can be determined from the observed color excess.

The above analysis was somewhat simplistic in that it only took into account dust's effect on the slope of the spectrum. By using more than two bands, one can also account for the change in curvature and obtain a more sensitive measure of both the dust extinction and color temperature, as was done by Clocchiatti et al. (1995) in their analysis of early-time SN 1993J spectra.

6. SUMMARY AND DISCUSSION

In § 1 we outlined a general procedure for deriving the color temperature and photometric angular size, θ, of Type II supernovae from broadband photometry. The value of θ is an essential ingredient needed for determining distances to SNe II with the Expanding Photosphere Method. The photosphere of SNe II are low density and scattering dominated; consequently, the emergent flux is dilute relative to the best-fitting blackbody spectrum. For EPM to work, one must know exactly how dilute the photospheric flux is, i.e., by how much the apparent distance must be multiplied to obtain the true value. The two most important results of this paper are the distance correction factors, ζ, presented in Figures 27–30 and in Table 5, and the demonstration that the relation of ζ to observable color temperature varies only slowly over a broad range of physical properties appropriate to SNe IIp.

This is an important problem because SNe IIp are observable to distances well beyond the local neighborhood at which the cosmological recession velocity is comparable to noncosmological anisotropies (e.g., SN 1992am [Schmidt et al. 1994a], which was observed at a distance of 180 Mpc). It has been our intent in this paper, therefore, to spell the problem out as concisely and with as much detail as would be necessary for others to reproduce the calculations we have performed and make use of the results we have presented. In § 2 we showed how simulation of the radiation field evolution in the photospheres of Type II plateau supernovae is much simplified by making use of the fact that the comoving frame luminosity is approximately constant above the diffusion depth, making it possible to replace the time dependent radiation transport equation with a much simpler radiative transfer equation. In the more general case in which L is changing rapidly, as it does in maximum light SNe Ia, the problem is explicitly time dependent and much more complicated to model.

In § 3 we described the two basic thermal and ionization structures of photospheric phase supernova atmospheres—hot and completely ionized, where cooling proceeds by a combination of diffusion and adiabatic expansion, and recombining, where the effective temperature equals the hydrogen recombination temperature and radiation is liberated by the action of an inward-moving recombination front. Numerous examples of spectra were presented which demonstrate some of the wide variety of behavior which can be had by changing the luminosity, chemical abundances, expansion rate, density, and density gradient.

Despite the large number of parameters which go into specifying our model atmospheres, and the correspondingly broad range of spectral behaviors they display, the distance correction factors themselves exhibit a behavior which is very nearly one-dimensional. The results of § 4 indicate that with good B, V, and I photometry, EPM can measure distances to SNe IIp with an accuracy of 5%–10% without having to craft custom atmosphere models for each set of observations. With B and V alone, the range of uncertainty is approximately doubled. Infrared photometry is free from the influence of line absorption, which dominates B-band–based color temperatures during the recombination epoch, and it should give results comparable to using optical photometry.

Two of our models, s15.5.1 and s25.5.1, display markedly different ζ behavior from the rest. In both these models the photosphere lies in the very outermost, highest velocity gas. The densities and effective temperatures are high in these models, and the density gradient is very steep. In both, but in s25.5.1 in particular, the emergent flux is nearly Planckian and undiluted. Although these models represent a very short lived evolutionary phase during which the photosphere is cooling rapidly and density dropping, it is conceivable that such conditions could be observed in SNe II if discovered shortly after explosion. If so, then the ζ values presented here should probably not be applied to those early observations, unless some method is devised to estimate the photospheric density.

A case in point is SN 1993J. Schmidt et al. (1993b) used preliminary values of the distance correction factors from this work to determine the distance to the peculiar Type II supernova SN 1993J. They derived a distance of 2.6 ± 0.4 Mpc, which should be compared to the value of 3.6 ± 0.3 Mpc obtained from *Hubble Space Telescope* observations of Cepheids in M81 (Freedman et al. 1994a). Clocchiatti et al. (1995) have studied the flux dilution and reddening in SN 1993J. One of their conclusions is that at very early times in SN 1993J, $\zeta \sim 1$. Their explanation for this is that as material in the low-density, extended envelope of SN 1993J was swept up by the shock, a narrow, optically thick shell formed which had a steep density gradient on the outside. Such a thin-shell structure is predicted by hydrodynamic

calculations (Shigeyama et al. 1994; Woosley et al. 1994). If so, then our results for conditions of high density are generally consistent with this explanation. We note, however, that such a shell would most likely have been Rayleigh-Taylor unstable and would have perhaps broken up into a number of clumps. SN 1993J, which has been described as a Type IIb supernova (Woosley et al. 1994), was very different from an SN IIp and from the models in this paper, and it is probably not a good candidate either for applying EPM or assessing its accuracy. As described by Woosley et al. (1994), these differences include the fact that the star's hydrogen envelope was only $0.20 \pm 0.05\ M_\odot$ and very helium rich. It had a nearby companion, was filling its Roche lobe at the time of explosion, and was thus highly deformed (major-to-minor axis ratio of 3:2). It was also likely to have been variable in luminosity and undergoing violent radial oscillations, all of which may have led to a significantly non-spherical explosion, violating one of the main assumptions of EPM—that of spherical symmetry. Baron et al. (1993) constructed custom atmosphere models for SN 1993J at two epochs and used the models to derive an EPM distance of 4.0 ± 0.5 Mpc. The difference between that number and the *HST* Cepheid distance may have been due in part to departures from spherical symmetry.

We recommend that the ζ values presented in § 4 be applied only to Type II plateau supernovae during the plateau phase. The common SNe IIp having a plateau duration of $\sim$80–150 days is most likely to have originated from a star of mass 10–20 $M_\odot$ which is sufficiently isolated so as to not have experienced substantial mass loss by Roche lobe overflow. Stars in this mass range are also not expected to have undergone excessive amounts of radiatively driven mass loss. The resulting supernova then will have $\sim 10\ M_\odot$ of hydrogen-dominated envelope and will be spherical to a high degree of accuracy, and of all the potential candidates for applying EPM to, the physics of plateau phase SNe IIp is the most well understood and easiest to model.

Compared to Type II plateau supernovae, other supernovae types are much less suitable for application of EPM, and this includes stars such as the peculiar Type II SN 1993J discussed above, as well as Type Ia supernovae (SNe Ia). These latter are perhaps the most problematic. The physics of SNe Ia is much less well understood than for SNe IIp and is far more difficult to model. In plateau phase SNe IIp, the major opacity contributor is hydrogen, whose atomic properties are known exactly. In SNe Ia, opacity is provided by elements of the silicon and iron groups whose atomic properties are determined much less accurately. The SN IIp plateau luminosity is provided by shock deposited internal energy which is released by a wave of inward-moving transparency. The thermal structure of this transparency or recombination wave is well understood and has been modeled accurately, in the present work and elsewhere. By comparison, SNe Ia are powered by ^{56}Ni and ^{56}Co radioactive decay. This decay energy is converted into far-ultraviolet photons near the center, where they are trapped by a thick forest of ultraviolet lines of Fe, Co, and Ni. A single UV photon scatters multiple times before it branches into several optical wavelength photons which can then diffuse outward on a short timescale. The Doppler shifts which these optical wavelength fluorescence photons experience as they diffuse outward creates the appearance of a smooth continuum spectrum, but it is not a thermal continuum spectrum, as it is in SNe IIp, and it bears little relation to the process which takes place at the photospheres of SNe IIp.

The ζ values from this paper have been applied in several previously published studies (Schmidt et al. 1993b, 1994a, b). Based upon the results of the present work, Schmidt et al. (1994b) derived a Hubble constant of 73 ± 7 km s^{-1} Mpc^{-1} from EPM distances to 18 SNe II. Although that determination did not bring an end to all debate on the value of H_0, we note nonetheless that it is in excellent agreement with subsequent determinations based on *HST* observations of Cepheid stars in M100 by Freedman et al. (1994b), who obtained $H_0 = 80 \pm 17$ km s^{-1} Mpc^{-1}. More recently, Tanvir et al. (1995) used *HST* observations of Cepheid stars in M96 to measure a distance to the Leo I group of 11.6 ± 0.8 Mpc. This value, when combined with relative distance information to more distant clusters, yields the value $H_0 = 69 \pm 8$ km s^{-1} Mpc^{-1}, which is in even better agreement with the SNe II EPM result.

There have not been any measurements of Cepheids in a galaxy which has previously hosted a Type II plateau supernova. However, Eastman & Kirshner (1989) determined an EPM distance of 49 ± 6 kpc to SN 1987A in the Large Magellanic Cloud which is in excellent agreement with studies based on observation of LMC Cepheids (Walker 1987; Feast 1991) and RR Lyrae stars (Walker & Mack 1988). Schmidt et al. (1994b) derive EPM distances to the two Type II *linear* supernovae SN 1970G in M100 ($D_{\rm EPM} = 7.4^{+1}_{-1.5}$ Mpc) and SN 1979C in M100 ($D_{\rm EPM} = 15 \pm 4$ Mpc), which, given the peculiar nature of these supernovae and that they are not SNe IIp, is in very good agreement with the Cepheid distances of 7.5 Mpc to M100 (Kelson et al. 1996) and 17.1 ± 1.8 Mpc to M101 (Freedman et al. 1994b).

Table 6 summarizes the current EPM distance scale and the corresponding six available Cepheid distances. Three of the six Cepheid distances are to galaxies in the same group as the SN II hosts and are marked accordingly. The two methods show remarkable consistency, $D_{\rm Cepheids}/D_{\rm EPM} = 0.98 \pm 0.08$, which suggests that any systematic differences between the two methods are very small. Several more Cepheid distances will become available in the coming year (also marked on the table), and it will be interesting to see if the EPM distance estimates for these galaxies will be replicated by the Cepheid measurements.

There are two additional very important tests which have been applied to EPM: first, the distance to an individual supernova, which is given by the slope of $\theta/v_{\rm ph}$ versus t (eq. [4]), should not change with time after explosion. Well-observed SNe IIp pass this test with flying colors (see, e.g., Fig. 6 of Schmidt et al. 1994a). The other test is the Hubble diagram test, and here again, the application of EPM to SNe II has been shown to reproduce Hubble's law at distances out to 180 Mpc (Schmidt et al. 1994a). Both Pierce (1994) and Schmidt et al. (1994b) compared EPM and Tully-Fisher distances to eight spiral galaxies and found $D_{\rm EPM}/D_{\rm TF} \approx 0.89 \pm 0.05$. Pierce goes on to conclude that EPM is at least as reliable for distance measurement as assuming that Type Ia supernovae are standard candles. Unlike standard-candle methods, however, EPM is less vulnerable to uncertainties in dust extinction (§ 5).

The result of the present work and that by Montes & Wagoner (1995) that the behavior of ζ_S with T_S varies only slowly with density is confirmed by the observation that SNe IIp produce consistent relative distances. The shape of our $\zeta_S(T_S)$ must then be very nearly correct. The only pos-

TABLE 6

EPM AND CEPHEID DISTANCES TO TYPE II SUPERNOVAE

SN	Galaxy	v_{rec}[a] ($km\ s^{-1}$)	v_{rec}[b] ($km\ s^{-1}$)	A_V (mag)	EPM Distance (Mpc)	Cepheid Distance (Mpc)
SN 1968L	NGC 5236	380	380	0.11	$4.5^{+0.7}_{-0.8}$	4.1 ± 0.4[c,f]
SN 1969L	NGC 1058	620	620	0.18	$10.6^{+1.9}_{-1.1}$	9.29 ± 0.69[e,f]
SN 1970G	NGC 5457	380	390	0.44	$7.4^{+1.0}_{-1.5}$	7.5 ± 0.8[c,f]
SN 1973R	NGC 3627	450	460	2.70	15^{+7}_{-7}	...
SN 1979C[d]	NGC 4321	1300	1150	0.45	15^{+4}_{-4}	17.1 ± 1.8[c,f]
SN 1980K	NGC 6946	320	310	1.20	$5.7^{+0.7}_{-0.7}$	...
SN 1986L[a]	NGC 1559	1110	1110	0.00	16^{+2}_{-2}	...
SN 1987A	LMC	...	...	0.60	$0.049^{+0.006}_{-0.006}$	0.051 ± 0.003
SN 1988A	NGC 4579	1300	1150	0.00	20^{+3}_{-3}	17.1 ± 1.8[c,f]
SN 1989L	NGC 7331	1420	1440	1.00	17^{+4}_{-4}	...[g]
SN 1990E	NGC 1035	1230	1240	1.70	18^{+3}_{-2}	...
SN 1990K	NGC 150	1420	1440	0.50	20^{+5}_{-5}	...
SN 1990ae.....	anon0020+06	7800	7800	0.50	115^{+35}_{-25}	...
SN 1992H	NGC 5377	2240	2150	0.00	31^{+4}_{-4}	...
SN 1992af	ESO 340-G38	5380	5400	0.00	55^{+25}_{-20}	...
SN 1992am.....	anon0122-04	14500	14500	0.30	180^{+35}_{-25}	...
SN 1992ba	NGC 2082	950	940	0.30	$14^{+1.5}_{-1.5}$	...

[a] Corrected for Virgo infall; $V_{Vir} = 1050\ km\ s^{-1}$, $V_{in} = 250\ km\ s^{-1}$.
[b] Corrected for Virgo infall; $V_{Vir} = 950\ km\ s^{-1}$, $V_{in} = 200\ km\ s^{-1}$.
[c] From Mould et al. 1995.
[d] Has peculiar spectroscopic features.
[e] From Silberman et al. 1996.
[f] Cepheid distance from group member.
[g] *HST* Cepheid distance forthcoming.

sible remaining systematic effect which could influence SNe IIp EPM distances is that the whole $\xi_S(T_S)$ curve in Figures 27–30 might be off by a constant vertical scale factor which is independent of T_S. However, the models in our study represent a very wide range of physical conditions, and it is unlikely that all our results would be off by the same constant scale factor. The consistent relative agreement with Tully-Fisher distance measurements, the good agreement found in the three cases in which direct comparison can be made with Cepheid distances, and the concordant results on Cepheid-based determinations of H_0 lead us to conclude that the distance corrections calculated in this paper are accurate, and that EPM, applied appropriately to SNe IIp, is a powerful and precise technique for studying the extragalactic distance scale.

We would like to thank the referee, Robert V. Wagoner, for his careful, critical reading of the manuscript and his highly constructive comments. R. G. E. thanks Stan Woosley, Tom Weaver, and Philip Pinto for their encouragement, numerous edifying discussions, and also for access to the KEPLER explosion models used in this study. This work was supported by the US Department of Energy (W-7405-ENG-48) and by the NASA Theory Program (NAGW 2525).

REFERENCES

Anders, E., & Grevesse, N. 1989, Geochim. Cosmochim. Acta, 53, 197
Anderson, L. S. 1989, ApJ, 339, 558
Ažusienis, A., & Straižys, V. 1969, Soviet Astron.-AJ, 13, 316
Baron, E., Hauschildt, P. H., Branch, D., Wagner, R. M., Austin, S. J., Filippenko, A. V., & Matheson, T. 1993, ApJ, 416, L21
Bessel, M. S. 1983, PASP, 95, 480
Branch, D. 1987, ApJ, 320, L23
Branch, D., Falk, S. W., McCall, M. L., Rybski, P., Uomoto, A. K., & Will, B. J. 1983, ApJ, 244, 780
Castor, J. 1972, ApJ, 178, 779
Chilikuri, M., & Wagoner, R. 1988, in IAU Colloq. 108, Atmospheric Diagnostics of Stellar Evolution: Chemical Peculiarity, Mass Loss, and Explosion, ed. K. Nomoto (Berlin: Springer-Verlag), 295
Chandrasekhar, S. 1961, Radiative Transfer (New York: Dover)
Chevalier, R. 1976, ApJ, 207, 872
———. 1992, ApJ, 394, 599
Clocchiatti, A., Wheeler, J. C., Barker, E. S., Filippenko, A. V., Matheson, T., & Liebert, J. 1995, ApJ, 446, 167
Eastman, R. G., & Kirshner, R. P. 1989, ApJ, 347, 771
Eastman, R. G., & Pinto, P. A. 1993, ApJ, 412, 731
Eastman, R. G., Woosley, S. E., Weaver, T. A., & Pinto, P. A. 1994, ApJ, 430, 300 (EWWP)
Falk, S. W., & Arnett, W. D. 1977, ApJS, 33, 515
Feast, M. 1991, in New Aspects of Magellanic Clouds Research, ed. B. Baschek et al. (Dordrecht: Kluwer), 239
Freedman, W. L., et al. 1994a, ApJ, 427, 628
———. 1994b, Nature, 371, 757
Grassberg, E. L., Imshennik, V. S., & Nadyozhin, D. K. 1971, Ap&SS, 10, 28
Herant, M., & Woosley, S. E. 1994, ApJ, 425, 814
Hershkowitz, S., Linder, E., & Wagoner, R. 1986a, ApJ, 301, 220
———. 1986b, ApJ, 303, 800
Hershkowitz, S., & Wagoner, R. 1987, ApJ, , 322, 967
Höflich, P. 1991, in Supernovae: The Tenth Santa Cruz Summer Workshop in Astronomy and Astrophysics, ed. S. Woosley (Berlin: Springer-Verlag), 415

Johnson, H. L. 1965, ApJ, 141, 923
Kalkofen, W. 1987, in Numerical Radiative Transfer, ed. W. Kalkofen (Cambridge: Cambridge Univ. Press), 1
Kelson, D., et al. 1996, ApJ, 463, 26
Kirshner, R. P., & Kwan, J. 1974, ApJ, 193, 27
Kurucz, R. L. 1991, in Stellar Atmospheres: Beyond Classical Models, ed. L. Crivellari, I. Hubeny, & D. G. Hummer (Dordrecht: Kluwer), 441
Li, H., & McCray, R. 1996, ApJ, 456, 370
Mihalas, D. 1978, Stellar Atmospheres (San Francisco: Freeman)
Mihalas, D., Kunasz, P. B., & Hummer, D. G. 1976, ApJ, 210, 419
Montes, M., & Wagoner, R. V. 1995, ApJ, 445, 828
Mould, J. R., et al. 1995, ApJ, 449, 413
Pennypacker, C., et al. 1990, IAU Circ. 4955
Pierce, M. J. 1994, ApJ, 430, 53
Pinto, P. A. 1988, Ph.D. thesis, Univ. California, Santa Cruz
Pinto, P. A., & Woosley, S. E. 1988, Nature, 333, 534
Savage, B. D., & Mathis, J. S. 1979, ARA&A, 17, 73
Schmidt, B. P., Kirshner, R. P., & Eastman, R. G. 1992, ApJ, 395, 366
Schmidt, B. P., Kirshner, R. P., Eastman, R. G., Phillips, M. M., Suntzeff, N. B., Hamuy, M., Aviles R., & Maza, J. 1994b, ApJ, 432, 42
Schmidt, B. P., et al. 1993a, AJ, 105, 2236
———. 1993b, Nature, 364, 600
———. 1994a, AJ, 107, 1444
Schmutz, W., Abbott, D. C., Russell, R. S., Hamann, W.-R., & Wessolowski, U. 1990, ApJ, 355, 255
Schurmann, S. R., Arnett, W. D., & Falk, S. W. 1979, ApJ, 230, 11
Shigeyama, T., Suzuki, T., Kumagai, S., Nomoto, K., Saio, H., & Yamaoka, H. 1994, ApJ, 420, 341
Silbermann, N. A., et al. 1996, ApJ, in press
Sobolev, V. 1960, Moving Envelopes of Stars (Cambridge, MA: Harvard Univ. Press)
Suzuki, H., & Nomoto, K. 1995, ApJ, in press
Tanvir, N. R., Shanks, T., Ferguson, H. C., & Robinson, D. R. T. 1995, Nature, 377, 27
Van Regemorter, H. 1962, ApJ, 186, 906
Wagoner, R. V. 1982, in Supernovae: A Survey of Current Research, ed. M. J. Rees & R. J. Stoneham, (Dordrecht: Reidel), 253
Walker, A. R. 1987, MNRAS, 225, 627
Walker, A. R., & Mack, P. 1988, AJ, 96, 1362
Weaver, T. A., Zimmerman, G. B., & Woosley, S. E. 1978, ApJ, 225, 1021
Weaver, T. A., & Woosley, S. E. 1993, Phys. Rep. 227, 65
Woosley, S. E., & Weaver, T. A. 1986, ARA&A, 24, 205
Woosley, S. E., Eastman, R. G., Weaver, T. A., & Pinto, P. A. 1994, ApJ, 429, 300
Yakeda, Y. 1990, A&A, 234, 343
———. 1991, A&A, 245, 182
Xu, Y. 1989, Ph.D. thesis, Univ. Colorado